International
Progress Report

IPR-01-09

Äspö Hard Rock Laboratory

Analysis of the in-situ principal stress field at the HRL using acoustic emision data

Will Pettitt
Calum Baker
Applied Seismology Consultants Ltd.

R Paul Young
Liverpool University

October 2000

Svensk Kärnbränslehantering AB
Swedish Nuclear Fuel
and Waste Management Co
Box 5864
SE-102 40 Stockholm Sweden
Tel 08-459 84 00
+46 8 459 84 00
Fax 08-661 57 19
+46 8 661 57 19

Äspö Hard Rock
Laboratory

Report no.	No.
IPR-01-09	F86K
Author	Date
Pettitt, Young	00-10-25
Checked by	Date
Derek Martin	
Rolf Christiansson	00-12-20
Approved	Date
Christer Svemar	01-08-15

Äspö Hard Rock Laboratory

Analysis of the in-situ principal stress field at the HRL using acoustic emision data

Will Pettitt
Calum Baker
Applied Seismology Consultants Ltd.

R Paul Young
Liverpool University

October 2000

Keywords: Rock mechanics, Rock stresses, acoustic emision

Executive Summary

Existing acoustic emission (AE) data, recorded during excavation of deposition holes in the Prototype Repository Tunnel (PRT) at the Äspö Hard Rock Laboratory (HRL), are used to test the validity of two possible orientations of the stress tensor. The first stress field orientation (labelled A) is an average of measurements conducted down the length of the ramp at the HRL. The second stress field orientation (labelled B) is from a set of measurements conducted in borehole KA3579G in the PRT at the 450m level. Stress field B has a significant (and unexplained) rotation compared to A, with repercussions for the predictions of the behaviour of the rock mass in the PRT and for interpretations of its response during experiments conducted there. In the process of doing this study the mechanisms by which AEs are produced around the deposition holes are also investigated with respect to their relationship to the geology and the active stress field. A self-consistent explanation of the AEs is presented.

Using AE source locations from around the deposition holes it is shown that AEs are produced primarily through the disturbance of pre-existing macroscopic fractures (in the immediate vicinity of the deposition hole wall) by concentrations of high compressive stresses. This produces distributions

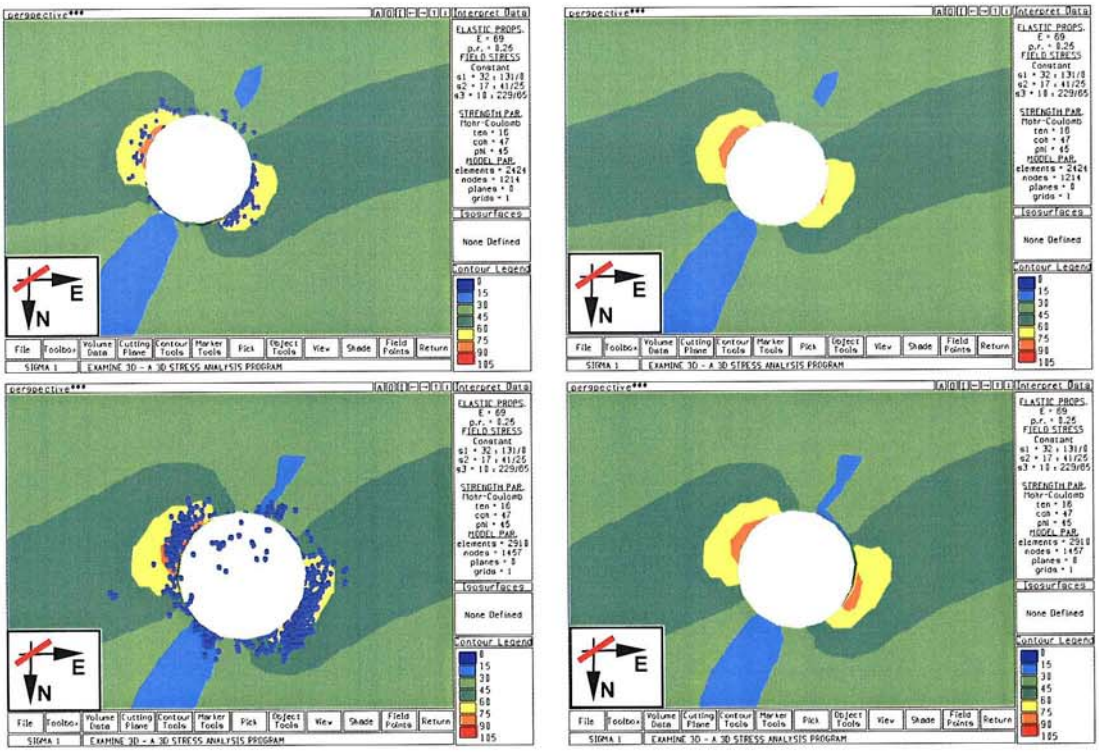

Comparison of AE locations with modelled induced stresses from measured stress field A. Upper two plots – DA3551G01. Lower two plots – DA3545G01. View is onto the tunnel floor from beneath.

of AEs in plan view that appear diametrically opposite, and therefore suggest potential 'breakout' zones. The exact mechanism by which AEs are produced may be a combined effect of generation of new microcracking in weakened zones of the rock mass close to the macroscopic fractures, and sliding generated by disturbance of pre-existing microcracks in this same region. When related to modelled stresses, the AE distributions fit very well with induced stress concentrations from measured stress field A. This relationship holds for all the deposition holes monitored in both the PRT and the

Retrieval Tunnels. In contrast, there is no clear relationship between the location of the AEs in the PRT and the induced stress concentrations produced by stress field B. AEs located in the floor of the deposition hole can also be explained by the localisation of high stress concentrations from measured stress field A but bear no relationship to measured stress field B.

AE source locations show that not every macroscopic fracture is disturbed sufficiently to generate AEs. The exception is for deposition hole DA3545G01 where almost every fracture intersected by the excavation produced activity. It is proposed that the walls of the deposition holes are in a critically stressed state and that small perturbations in the amount of disturbance are sufficient to switch-on the activity. During excavation of the deposition holes in the Retrieval Tunnel, AEs were observed to locate around one deposition hole when its neighbour was being excavated. Stress models have been produced to test whether two deposition holes result in a combined disturbance. These models show that the induced stress fields of the two neighbours are linked. When three deposition holes are excavated in a line the central deposition hole has a loading of +2.5MPa (approximately 3%), in regions parallel to the tunnel axis, compared to if it had no neighbours. This combined disturbance is related to the distances between the two deposition holes, the rock mass behaviour, the geometry of the tunnel above, and the orientations of the excavations with respect to the stress field, and so is likely to be different for different excavation designs. The effect of this should therefore be carefully considered in future repository designs.

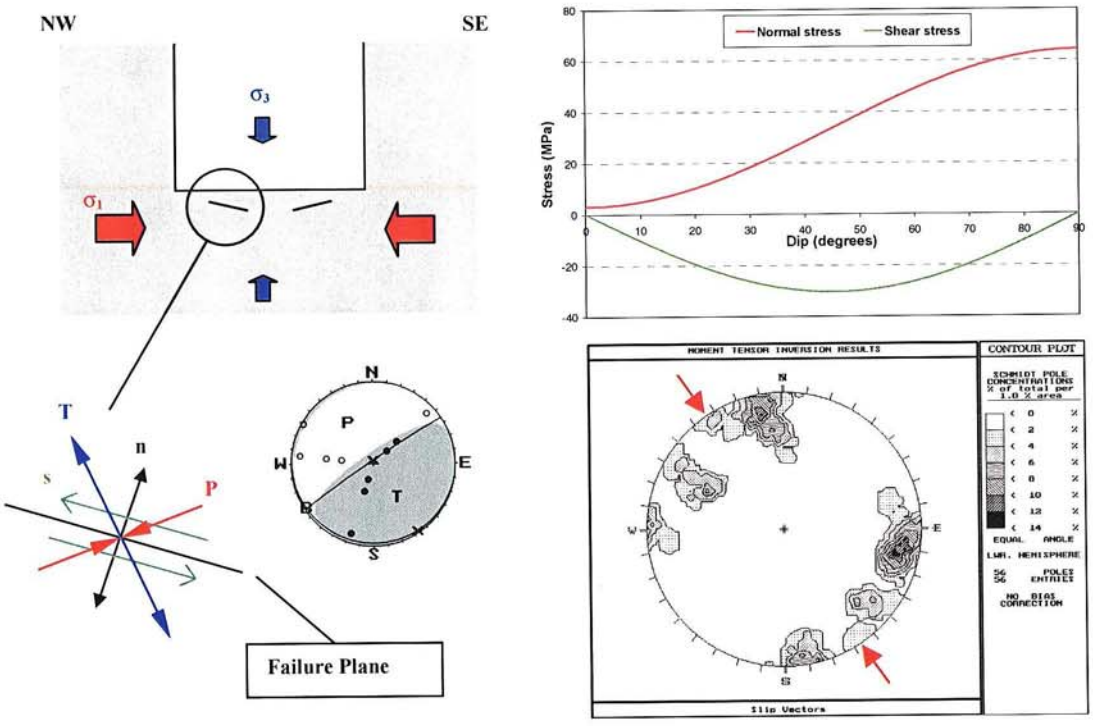

AE source mechanism results show a dominant mechanism type (left) on sub-horizontal fractures. Slip is activated due to low normal stresses (upper right). Slip vectors are preferentially orientated in the southest-northwest quadrants of the lower hemisphere. These results correlate very well with the orientation of the measured stress field A.

AE source mechanisms have been obtained for AEs occurring in the floor of excavation steps during the excavation of deposition hole DA3545G01. The AEs correspond to 'failure' on microcracks of the order of millimetres in dimension. 'Failure', in this case, corresponds to an adjustment, creation, or extension of a single microcrack in the rock. The source mechanisms describe the orientation and type of failure that is occurring. The observed mechanisms have a dominant type and relate to microcracks that are orientated sub-horizontal, and therefore sub-parallel to the surface of the excavation. Stress models show that the orientations of σ_1 and σ_2 in the floor of the deposition hole are horizontal and approximately retain their far-field azimuths; σ_3 is then vertical and into the void. The modelled σ_1

and σ_2 are therefore sub-parallel to the plane of the fractures. Slip is enabled on these fractures because σ_3 (and hence the normal stress on the fractures) tends to zero when the fractures are close to the deposition hole floor. The shear stress on these fractures is then a function of σ_1 and σ_2 resolved onto the fracture planes at acute angles. Slip vectors from the source mechanisms show that movement is orientated in the northwest and southeast quadrants on the lower hemisphere. This general movement direction is consistent with that expected from the orientation of measured stress field A. Hence, both the AE source mechanism and source location data show a better correlation with stress field A than with stress field B.

We have used a method of inverting for the stress field, local to the floor of deposition hole DA3545G01, using the available source mechanisms, but have found this data to provide an inconclusive result. This is mainly due to the ambiguity in the sense of slip observed in the mechanisms, but also due to scatter in the source mechanism results. However, the strong correlation between the modelled stress concentrations and the AE source location concentrations, and the correlation between the AE source mechanism orientations and the far-field stress orientations, indicates that the far-field in situ stress tensor orientation is more closely aligned to measured stress field A than stress field B. This result agrees with recently revised stress measurements from the PRT.

Contents

1 Introduction

In this study we utilise existing acoustic emission (AE) data to provide information on the principal-stress field active at the 450m level of the Äspö Hard Rock Laboratory (HRL). The AE data used here was primarily obtained during experiments conducted in the Prototype Repository Tunnel (PRT) during excavation of deposition holes there [*ASC*, 1999b]. Data will also be used from similar experiments conducted in the Retrieval Tunnel at the 420m level [*ASC*, 1999a] for the purposes of comparison. Figure 1-1 shows the positions of the PRT and the Retrieval Tunnel in the HRL.

Stress measurements in the PRT have provided an analysis of the far-field principal stress field that are inconsistent with measurements from elsewhere in the HRL. These principal stress measurements have been included as parameters in models for the mechanical response of the PRT excavations during excavation and subsequent operation. However, the ambiguity in the measurement of the far-field stress field must cause uncertainties in the modelling of induced stresses around the proximity of the PRT. This must in turn cause uncertainties in predictions for the behaviour of the rock mass, and interpretations of its response, during the PRT Experiment and during any further experiments conducted at the HRL. It is therefore of great importance that the condition of the stress field at the HRL is resolved accurately and unambiguously.

AEs, along with other seismic activity, are highly dependent on the excavation-induced stress field, as the mechanisms by which they are created rely on the orientations and magnitudes of stresses; either through their application to an existing fracture plane, or through compressive stresses being sufficiently high to provide fracture initiation, or through unloading of stresses being sufficient to cause fracture opening. The relationship between induced seismicity and underground excavations has been examined extensively at AECL's Underground Research Laboratory (URL), Canada [*Martin and Chandler*, 1994]. Experiments in this highly controlled environment have provided significant understanding of this relationship. We apply techniques utilised at the URL (adapted from crustal

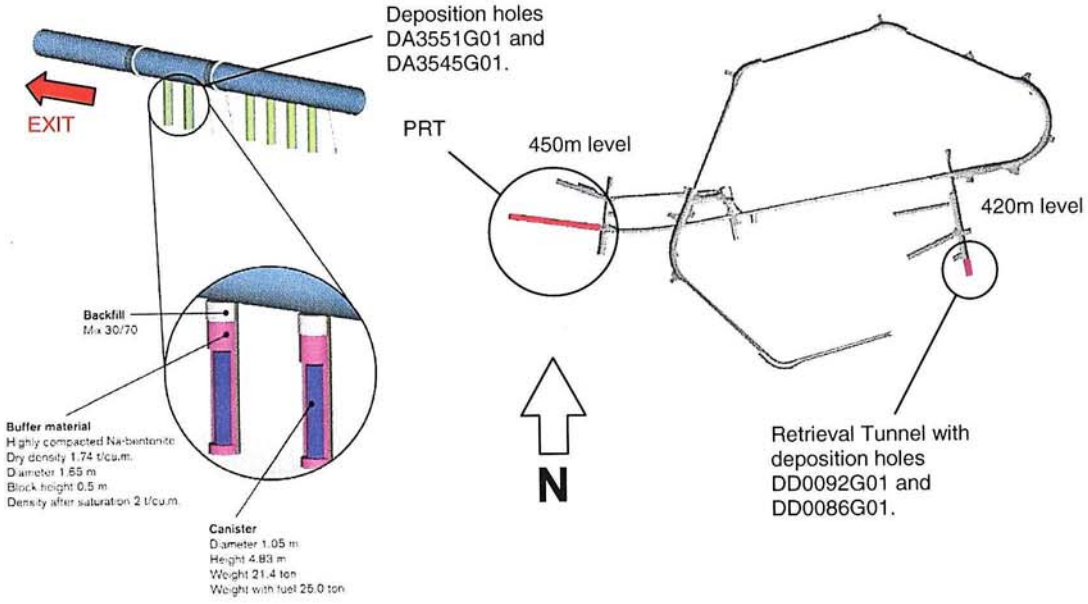

Figure 1-1: Plan view of the experimental tunnels at the Äspö HRL. *The locations of the PRT and Retrieval Tunnel are highlighted. A schematic illustration of the final experimental set up in the PRT is shown with canisters and bentonite clay installed in the two monitored 1.75m diameter deposition holes. Note the entrance of the tunnel is towards the left. Graphics are modified from SKB[1999].*

seismicity) to AEs recorded during the excavation phase of deposition holes in the PRT. In so doing we give further insights into the nature of the stress field at the HRL.

2 Background Information on the Stress Field at the HRL

The rock mass at the 450m level is predominantly massive Äspö diorite. *Patel et al.*[1997] have performed detailed mapping of discontinuities in the Prototype Repository tunnel. Two main discontinuous sets of sparse, en-echelon, fractures were observed. The principal fracture set is steeply dipping orientated to the West-Northwest (Figure 2-1a). This is regarded as the main water-bearing set. Sparsely located fractures are also observed with sub-horizontal dips and with steeply dipping North-south orientations. Similar fracture sets were found in the ZEDEX tunnels at the 420m level and are believed to be characteristic of the HRL volume.

Leijon[1995] summarises the stress magnitudes and orientations measured in boreholes at various locations down the HRL ramp using a CSIRO cell. Orientations are summarised in Figure 2-1b. Note there is a strong agreement between the maximum principal stress (σ_1) and the orientation of the principal fracture set. *Young et al.*[1996] note this agreement at the HRL and elsewhere, and use an average *in situ* stress tensor (*Table 2-1*) for the 420m level, calculated from the results of *Leijon*[1995], to model stress magnitudes induced around the ZEDEX tunnels. *Young et al.*[1996] analyse stress measurements conducted in the pillar between the two ZEDEX tunnels and relate these to predicted stresses. The authors show that stress magnitudes and orientations are often influenced by the close proximity of fractures to the measurement locations. A relationship that was also observed by *Martin and Chandler*[1993]. *Young et al.*[1996] question the validity of the *in situ* stress results of *Ljunggren and Klasson*[1996] using a Borre Probe on this basis. These results show dissimilar measurements in the ZEDEX volume to that presented by *Leijon*[1995]. The stress measurements of *Table 2-1* will be referred to as 'Far-field Stress Measurements A'.

Stress Component	Magnitude (MPa)	Trend (°)	Plunge (°)
σ_1	32	131	0
σ_2	17	41	25
σ_3	10	229	65

Table 2-1: Measured stress Field A: Principal stress values for the 420m level. These results are an average stress tensor for the 420m level calculated from data originally reported by *Leijon*[1995].

Stress Component	Magnitude (MPa)	Trend (°)	Plunge (°)
σ_1	34	188	39
σ_2	18	94	6
σ_3	13	356	51

Table 2-2: Measured stress Field B: Principal stress values measured in the Prototype Repository *[Ljunggren and Bergsten, 1998]*. The results are from a vertical borehole at 470m depth, approximately 20m beneath the tunnel floor.

Ljunggren and Bergsten[1998] give *in situ* stress measurements from a vertical borehole in the Prototype Repository. Four measurements were performed using a Borre Probe between 20 to 23m distance from the tunnel floor (outside the zone of influence from the tunnel). The mean principal stress magnitudes and orientations are given in *Table 2-2*. These are very similar in magnitude to *Table 2-1*, but are rotated in both azimuth and plunge (57° azimuth and 39° plunge) and are out of

character with other measurements conducted at the HRL. The reason for this rotation is unclear. The stress measurements of *Table 2-2* will be referred to as 'Far-field Stress Measurements B'.

For the PRT the significance of the rotated σ_1 is shown in Figure 2-1b. For field A σ_1 is at 33° azimuth from the tunnel orientation, which has an axis orientated 98° azimuth from North and 1.2° plunge towards the east. In field B, σ_1 is at 90° azimuth. This means that σ_1 must have a much larger effect on the excavations in field B than field A.

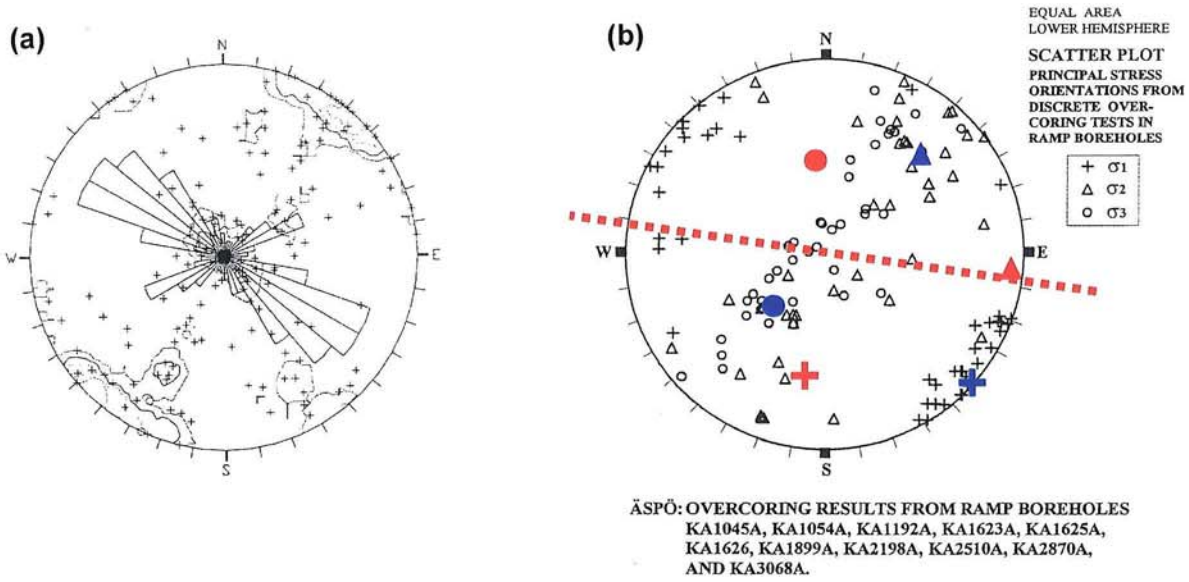

Figure 2-1: a) Pole, contour and rosette plot of joints from detailed mapping of the PRT performed by Patel et al.[1997]. b) Principal stress orientations measured from boreholes excavated from the HRL ramp (black markers) and summarised in Leijon[1995]. *Blue markers are far-field stress measurements A (***Table 2-1***). Red markers are far-field stress measurements B (***Table 2-2***). The dashed line is the azimuth of the PRT.*

3 Objectives

There are three principal objectives of this study.

1. Ascertain the relationship of AE clusters imaged around the deposition holes with structures intersected by excavation (such as pre-existing macroscopic fractures and lithological changes).
2. Examine the relationship between AE distributions around the deposition holes with modelled induced stresses. Determine which of the measured principal stress field orientations most closely explains the AE distributions.
3. Use AE source mechanism information (fault-plane solutions) calculated from recorded waveforms to estimate the far-field principal stress field, or to discriminate between the measured stress fields.

4 Results

4.1 Objective 1: Relationship of AE clusters with geological structures

4.1.1 AE maps in the PRT

ASC[1999a] and *ASC*[1999b] give AE locations monitored during excavation of deposition holes in the Retrieval Tunnel and PRT respectively (Figure 4-1 and Figure 4-2). The deposition holes have a diameter of 1.75m. AE locations have an estimated uncertainty of 10cm. We have taken locations from the deposition hole walls and superimposed them onto geological maps provided by SKB. In the case of the PRT, the AE map for deposition hole DA3545G01 is shown in Figure 4-3 and for DA3551G01 in Figure 4-4. The map is an unwrapped cylinder defining the interior of the deposition hole. The line passing through A to D defines the axis of the PRT with A orientated towards the tunnel entrance. AEs located below the floor of each 0.8m excavation step have been ignored. It should be noted that some of the AEs locate deeper into the walls (generally a maximum of 20cm) and so may be slightly misaligned to structures intersecting the surfaces, especially with those structures orientated near to the vertical.

The AEs in Figure 4-3 and Figure 4-4 describe two vertical distributions at approximately 140° azimuth and 320° azimuth. These were noted in *ASC*[1999b] as probable 'breakout' zones associated with high compressive stresses. The term 'breakout' is used loosely as the scale of the microcracking associated with the AEs is on the millimetre scale and is unlikely to be visible macroscopically. Only where intense activity is observed may damage be physically visible. Section 4.2.3 further investigates the relationship between the induced stresses and the AE locations.

Within the 'breakout' zones, AEs tend to localise into distinct clusters of 10-30cm in dimension. The main clusters have been interpreted from the location data and are shown on the AE maps of Figure 4-3 and Figure 4-4. In the PRT these clusters tend to be aligned with small volumes of rock that are bounded by intersections of two or more mapped macroscopic fractures. This is particular true for tight clusters; e.g. Cluster "1" highlighted on Figure 4-3. Other clusters (e.g. Clusters "2" and "3") are related to the intersection of the 'breakout' zone with the trace of individual macroscopic fractures on the walls. Clusters "2" and "3" are associated with horizontally orientated fractures near the floor of the fully excavated deposition hole. There is no apparent relationship between fracture orientation and the distribution of AEs. For deposition hole DA3545G01 almost every intersected fracture that passes through the 'breakout' zone has some AE activity associated with it, although the abundance of AEs is variable. It is rare to find clusters of AEs that cannot be associated with a fracture. This suggests that fractures play a significant role in the location of the AEs (and hence microcracking), and that the rock mass generally is sufficiently strong, compared to induced stresses, that microcrack initiation would not otherwise occur.

For deposition hole DA3551G01 in the PRT (Figure 4-4) - and also for deposition holes in the Retrieval Tunnel described in the following section - the majority of fractures do not generate clusters of AEs. It is therefore not true that all fracture intersections, or individual fractures, create AE clustering. There must therefore be some other mechanism (other than just excavation of the deposition hole through a fracture) that causes AEs to be induced in the 'breakout' zones. The AEs generated must be primarily due to concentrations of induced stresses or else these zones would not be apparent, however there must be a trigger that causes some fractures to be more disturbed than others. In the case of DA3545G01 all the fractures were systematically disturbed. There are a number of possible explanations that may play a subtle part in the abundance of AEs monitored. These include subtle differences in induced stresses, slight lithological variations (veins etc), small changes in monitoring array sensitivity, the water conductivity of fractures, fracture orientation in relation in local stress orientations, or the action of the cutter-head on the Tunnel-Boring Machine (TBM). Deposition hole DA3551G01 was excavated before DA3545G01 and shows the lower abundance of AEs, which suggests that one or more of these explanations subtly changed between the two deposition holes.

Assuming the changes between the two excavations were small then, for this change in AE activity to occur, the rock mass must be in such a critically stressed state that small changes in the experimental conditions caused the switching-on of the AE activity.

4.1.2 AE maps in the Retrieval Tunnel

Processing of the AE data from the PRT for source locations was performed using a combination of automatic processing, with manual checking of the travel-time picks for each AE, to remove or change inaccurate picks (see *ASC*, 1999b). AE processing from the Retrieval Tunnel, performed before the PRT experiment, was done using automatic picks alone. From the PRT data we observed that the AE locations had much smaller uncertainties, reducing scatter in the locations. We have re-processed the AE data from the Retrieval Tunnel using an identical approach to that performed in the PRT in order to provide AE source locations with consistent uncertainties. This has produced AE locations (Figure 4-2) with less scatter than shown in *ASC*[1999a]. It has not changed their general distributions, either spatially or temporally, and so does not change any of the observations or conclusions made in *ASC*[1999a]. We have used these enhanced locations in this analysis to compare with geological mapping of the deposition holes.

One striking feature from the locations of Figure 4-2 is the linear feature that intersects deposition hole DD0092G01 with an approximate strike of 70° East of North and a dip of 50°NNW. The view shown in Figure 4-2 looks along the strike of this feature. Figure 4-5 shows an equivalent map for deposition hole DD0092G01 in the Retrieval Tunnel to those described for the PRT in the previous section. The AEs delineating this feature are associated with a highly fractured zone mid-way down the deposition hole (marked in blue). A similar fracture zone exists just beneath the tunnel surface on which sporadic AEs are located (marked in green). A very dense cluster of AEs (labelled Cluster "4") is associated with a vein (labelled 'B4' - Pegmatite - by the geologist). Lithological controls on seismicity were observed at the Mine-by experiment in the URL and are discussed by *Collins and Young*[2000]. Sharp contrasts in elastic properties between the vein and the material around it may explain microcracking in the vein. AE clusters are less evident in deposition hole DD0086G01 (Figure 4-6) probably because the highly fractured zone in DD0092G01 is not apparent in this case.

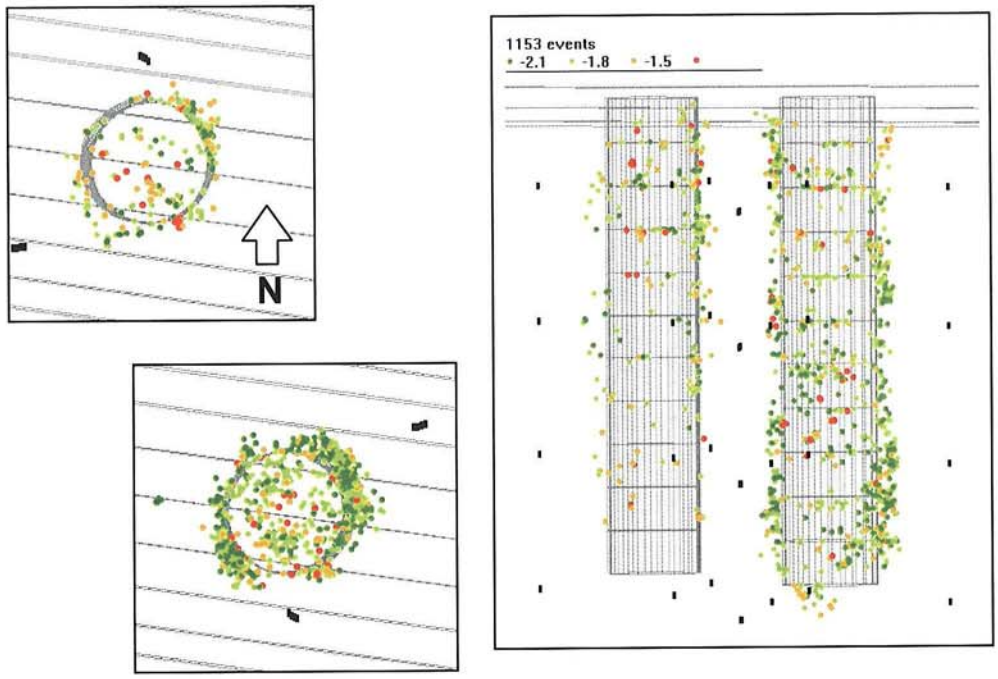

Figure 4-1: AE locations obtained from monitoring of deposition hole excavation in the PRT. *Left: Plan views of deposition hole DA3551G01 (upper) and DA3545G01 (lower). Right: View looking along horizontal and northwest.*

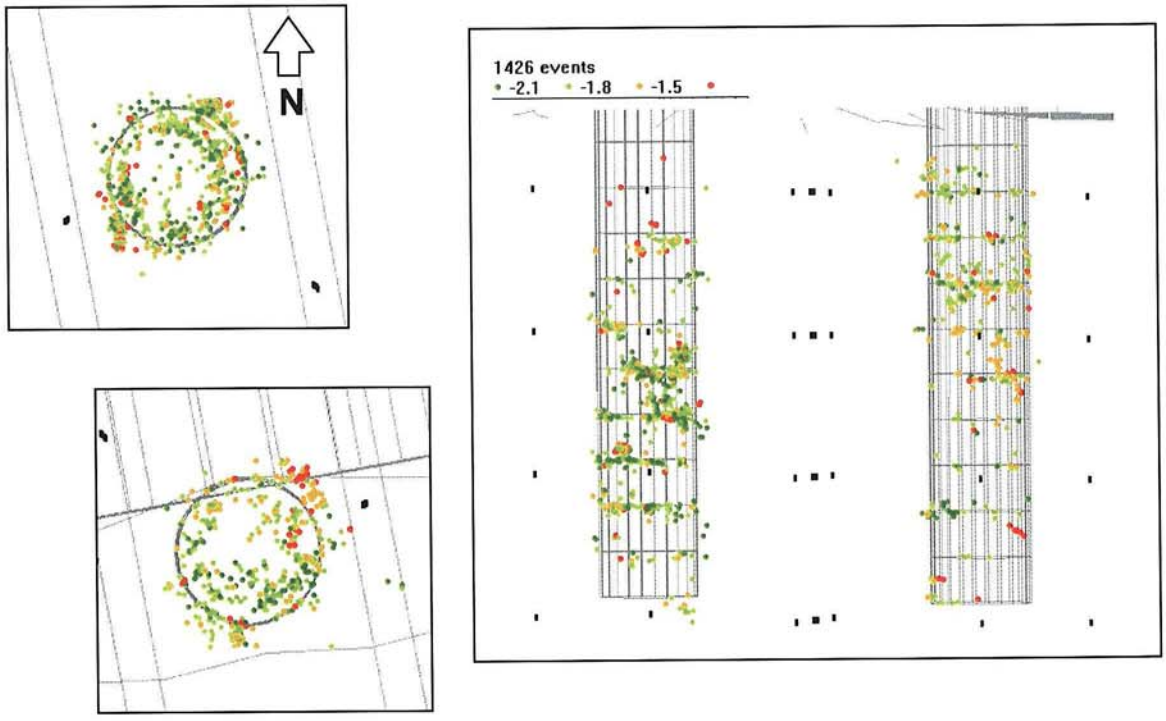

Figure 4-2: AE locations obtained from monitoring of deposition hole excavation in the Retrieval Tunnel. *Left: Plan views of deposition hole DD0092G01 (upper) and DD0086G01 (lower). Right: View looking along horizontal and west-southwest.*

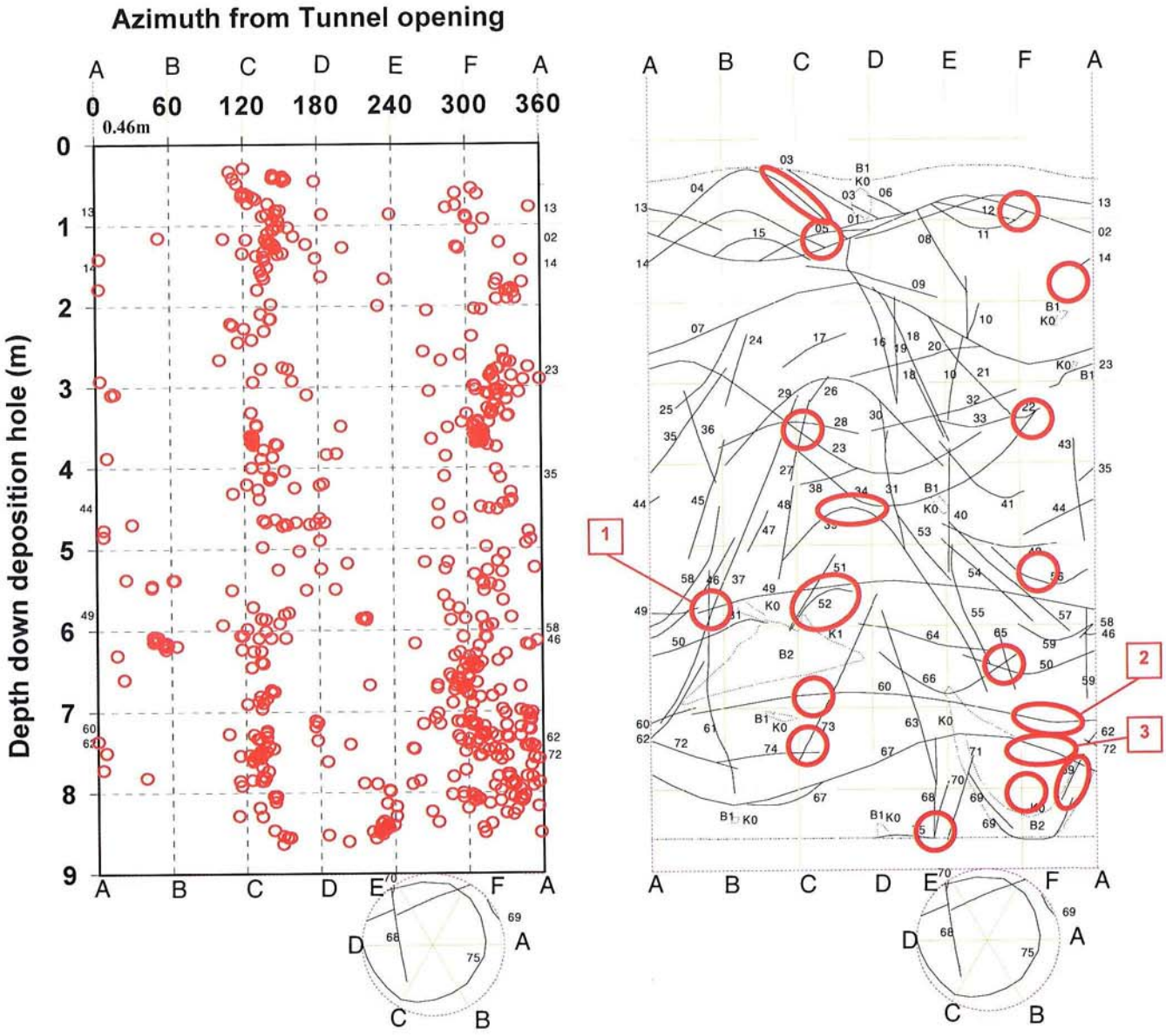

Figure 4-3: AE map of activity in the walls of deposition hole DA3545G01 (PRT) superimposed onto a geological map provided by SKB [Hardenby, 2000]. *Left: Scatter plot of activity. Right: Interpreted AE cluster locations.*

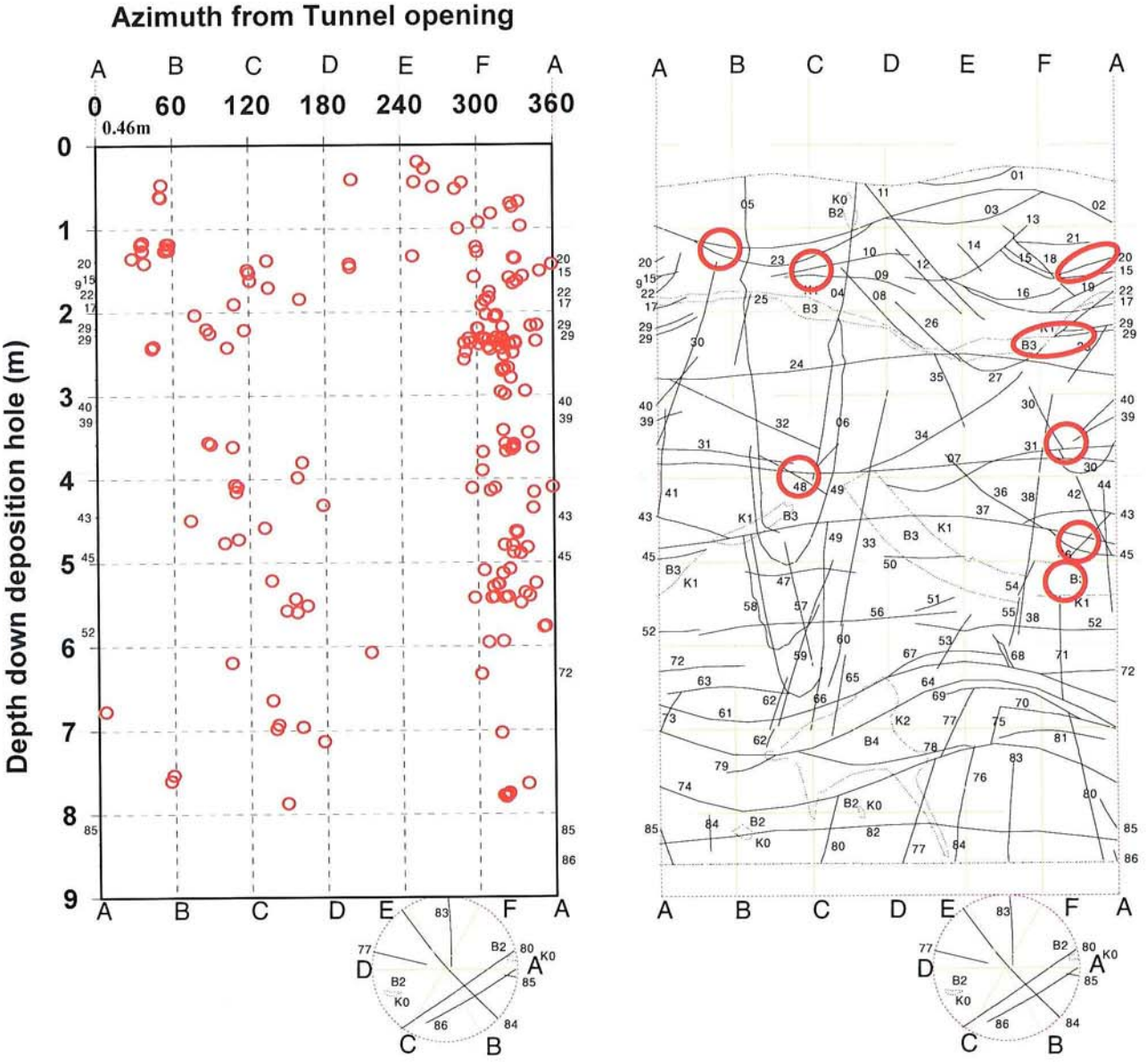

Figure 4-4: AE map of activity in the walls of deposition hole DA3551G01 (PRT) superimposed onto a geological map provided by SKB [Hardenby, 2000]. *Left: Scatter plot of activity. Right: Interpreted AE cluster locations.*

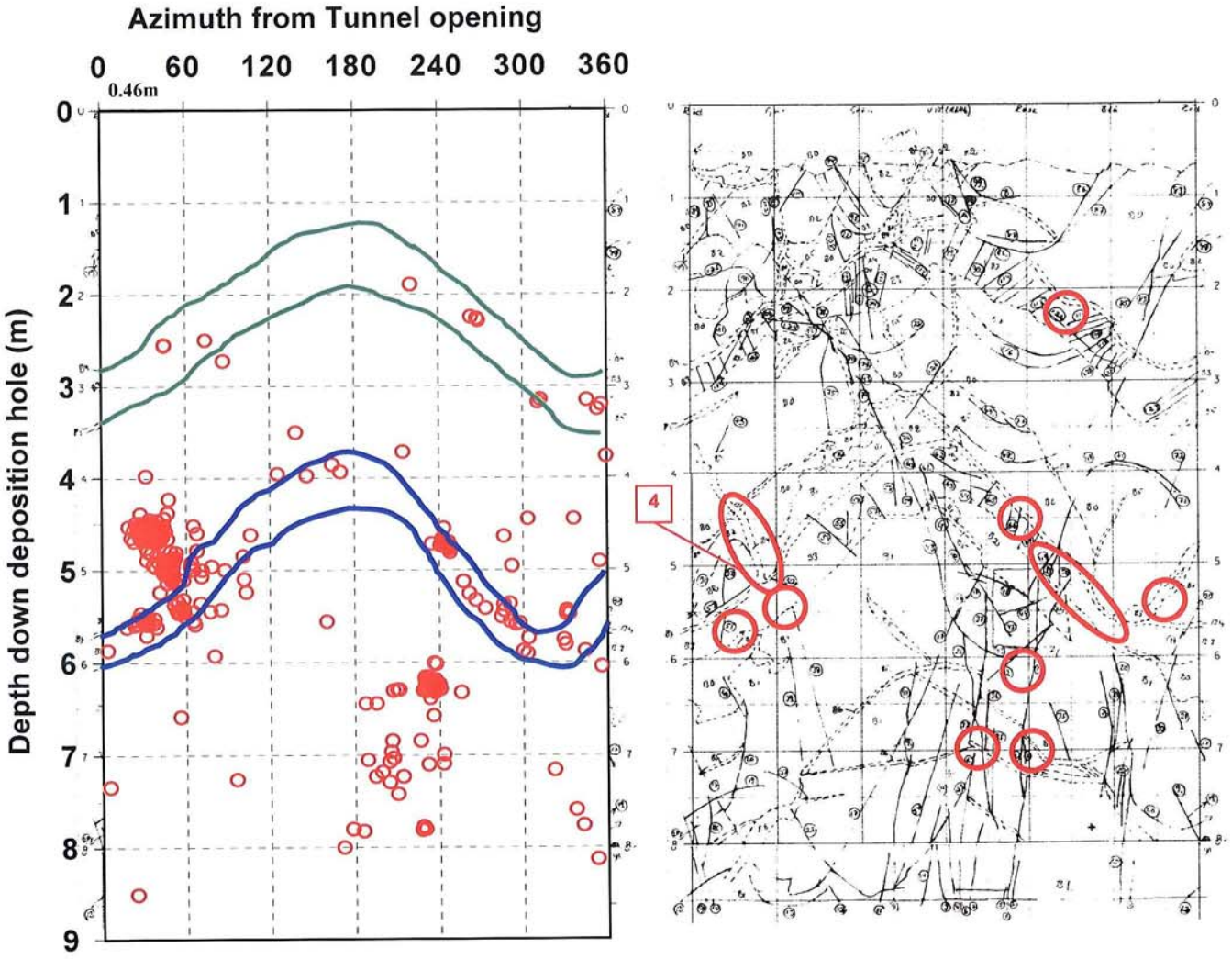

Figure 4-5: AE map of activity in the walls of deposition hole DD0092G01 (Retrieval Tunnel) superimposed onto a geological map provided by SKB [Hardenby, 2000]. *Left: Scatter plot of activity. Right: Interpreted AE cluster locations.*

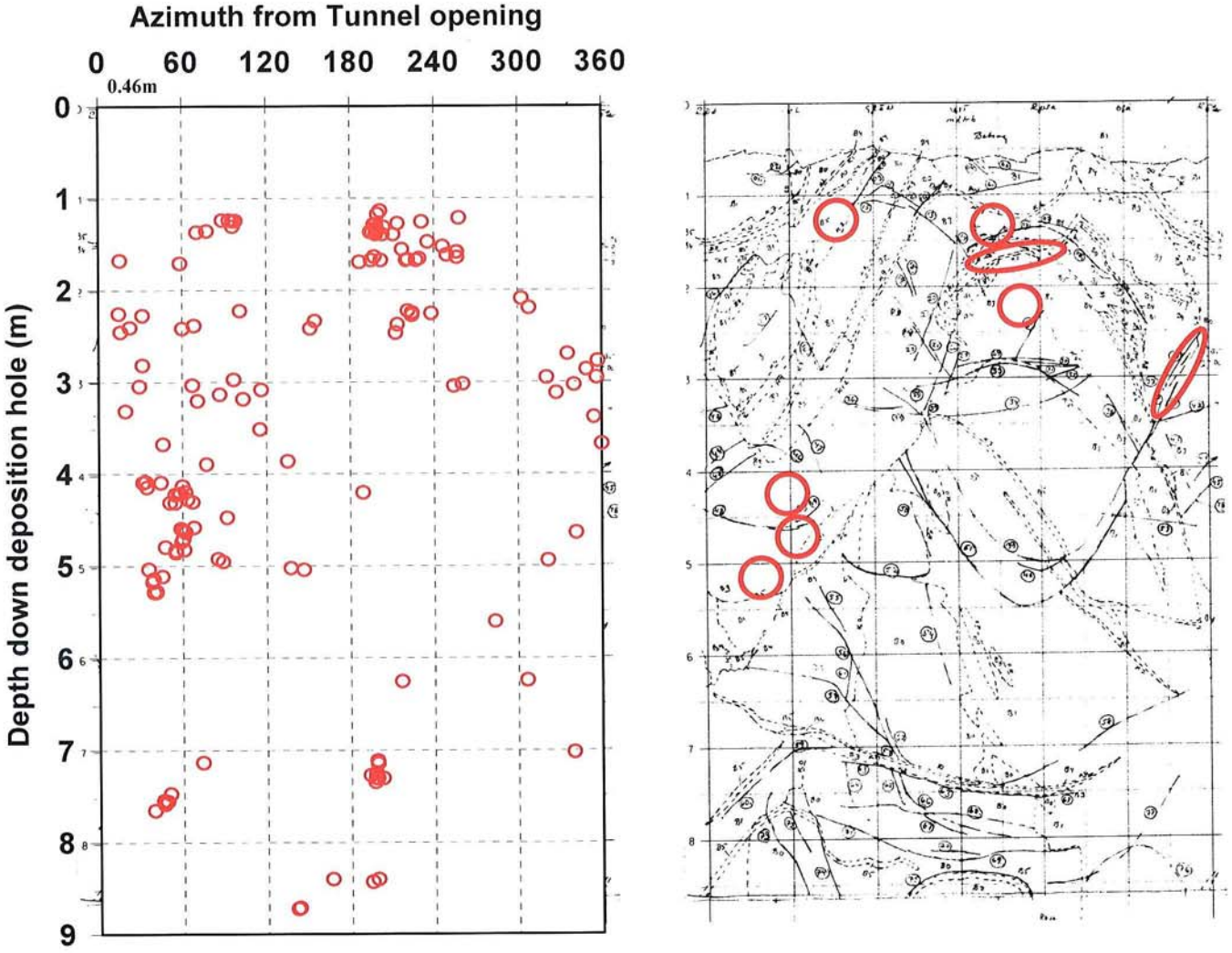

Figure 4-6: AE map of activity in the walls of deposition hole DD0092G01 (Retrieval Tunnel) superimposed onto a geological map provided by SKB [Hardenby, 2000]. *Left: Scatter plot of activity. Right: Interpreted AE cluster locations.*

4.2 Objective 2: Discrimination of the stress field orientation using AE source locations

4.2.1 The relationship between AE locations and stress disturbance

The relationship between seismicity and induced stresses has been investigated at the URL. There is a high spatial correlation between microseismic events (and AEs) and concentrations of induced compressive stresses [*Martin and Chandler*, 1994; *Young et al.*, 2000]. During the Mine-by experiment, induced compressive stresses of up to 150MPa in the roof and the floor of the tunnel caused the formation of breakout notches. This failure is equivalent to borehole breakout observed in highly stressed environments, and is orientated orthogonal to the maximum far-field principal stress (σ_1) direction. A damage initiation criterion for the rock mass at the URL has been established as σ_1-$\sigma_3 \approx 70$MPa at which AEs and microseismic activity begins to occur. The introduction of new cracks in the breakout zone is associated with induced stresses passing through this *in situ* crack-initiation stress, similar to cracking observed in laboratory samples under compressive loading.

In addition to this effect, seismic activity can be initiated on existing fractures when the normal and shear stresses are such that slip can occur. This is highly plausible in an environment where stresses local to pre-existing fractures are changing due to excavation of nearby voids. Unloading of stresses normal to the fracture, or loading of shear stresses parallel to the fracture, may enable slip. This effect is discussed by *Emsley et al.*[1997] for the ZEDEX at the HRL. In a similar manner, the introduction of increased pore pressures on the fracture surface will act to reduce the effective normal stress and may induce slip. *Emsley et al.*[1997] also discusses the unloading of a rock mass as a mechanism for crack extension. In this case, when the ratio of σ_3/σ_1 drops to below approximately 0.1, pre-existing cracks can be extended. During ZEDEX it was observed that there was a much larger occurrence of AEs around a tunnel excavated by 'drill-and-blast' than by a TBM (where very little activity occurred). Stress modelling showed induced stresses were probably insufficient to create crack-initiation around the tunnels. Instead, new cracks were introduced into the rock mass by the excavation method itself (drill-and-blast causing much greater disturbance than a TBM). AEs then occurred on these new fractures, due to crack extension from unloading of stresses, and due to shear sliding.

Whatever the mechanism, AEs at the PRT are primarily a result of a disturbed stress field due to the excavation of the nearby voids. Knowing the AE locations, and by modelling induced stresses around the excavations, it should be possible to discriminate between the far-field stress fields A and B. This is the approach we take here. We begin by making the assumption that AEs are created through the introduction of high compressive stresses, and hence the introduction of new crack initiation. This assumption is verified in later sections.

To model induced stresses local to the PRT excavations we have used the boundary-element stress-modelling package, Examine^{3D} [*Curran and Corkum*, 1993]. Three-dimension models of the excavations in the PRT have been constructed, and then induced stress magnitudes and orientations have been computed over the excavation boundaries (and through a volume around the excavations) for each of the far-field stress fields A and B. The models assume (by definition) an infinite elastic medium outside of the excavation volume. Hence effects of geological structures such as macroscopic fractures and changes in lithology are ignored in this analysis. The models use elastic properties for Äspö Diorite from *Patel et al.*[1997] Table 6-2 with Young's Modulus, E=69GPa and Poisson's Ratio, ν=0.25.

4.2.2 Stress models of the PRT

Figure 4-7 and Figure 4-8 show stress analyses for the PRT using stress field A and B respectively. The tunnel has a diameter of 5m with an axis extending between (264.381m North, 955.780m East, 447.371m Down) and (277.310m North, 866.289m East, 445.449m Down). This is measured from the entrance to the face of the PRT. A cutting plane is shown in each of the plots at 918m East, approximately between the collars of the two deposition holes, DA3545G01 and DA3551G01. It should be noted that the length of the model is such that the entrance of the PRT (modelled as a tunnel face) is sufficiently far from the deposition hole volume that it has negligible effect. The two figures have the same stress scale.

For stress field A, the maximum principal stress is induced to a maximum of 53MPa in the roof and floor of the PRT. In this case the far-field σ_1 and σ_2 are approximately horizontal and hence act to induce increased compressive stresses around the PRT in the vertical direction. In contrast, stress field B has an induced maximum principal stress of 78MPa (a 50% increase) orientated at approximately 45° to the vertical. This is largely a result of the far-field σ_1 being rotated in this case to an orientation orthogonal to the tunnel and at an increased plunge. For both stress fields A and B the minimum principal stress reduces to zero on much of the tunnel perimeter. For field A there is a tensile zone (σ_3<0) observed ahead of the face.

4.2.3 Stress models for deposition holes in the PRT

Figure 4-9 through to Figure 4-12 show stress analyses for the PRT with completed excavations of the two deposition holes DA3551G01 and DA3545G01. The value of induced σ_1 is shown. The value σ_1-σ_3 is very similar in both magnitude and distribution. Stress effects of the four other deposition holes (DA3569G01 through to DA3587G01) also excavated in the tunnel are ignored (the closest is at a radial distance of 18m). The effect of neighbouring deposition holes on stress distributions is discussed in Section 4.2.5. Figure 4-9 and Figure 4-11 show stress analyses for the two deposition holes using Field A. Stress concentrations are diametrically opposite, and observed approximately orthogonal to the far-field σ_1 azimuth (indicated by red line on lower plots), although there is a small rotation of approximately +15° azimuth. The stress rotation is a three-dimensional (3D) effect of the tunnel-deposition hole geometry. The angle of rotation reduces down the deposition hole length (with distance from the tunnel) so that the stress concentrations close to the floor of the deposition hole are orientated orthogonal to the far-field σ_1. This is a good example of the requirement for truly 3D stress analyses. The maximum stress observed is 97MPa in the intersection between the deposition hole and the Prototype Tunnel. For both deposition holes the orientation of high stress concentrations match very closely with distributions of AE locations observed during excavation of the deposition holes (blue markers). The distributions also appear to be rotated, following the modelled 3D stress field and are not exactly orthogonal to the far-field σ_1 as may be expected without the 3D analysis.

Figure 4-10 and Figure 4-12 show stress analyses for the two deposition holes using Field B. In this case the orientation of the far-field stress field induces stresses around the excavations that are notably asymmetric with respect to the deposition hole axis. Low stresses of 15-30MPa are observed to the south of the deposition hole and high stresses of >30MPa to the north. This is due to the effect of the far-field σ_1 (with a plunge of 39° to the horizontal) on the tunnel geometry, as shown in Figure 4-8. Orientations of high stress concentrations around the deposition hole perimeter are orthogonal to the far-field σ_1 azimuth, lying in an east-west orientation, but are not perfectly diametrically opposite. The maximum stress observed is 104MPa in the intersection between the deposition hole and the Prototype Tunnel. When compared to the AE locations the stress concentrations show a very low correlation with the AE distributions.

4.2.4 Stress models for deposition holes in the Retrieval Tunnel

It is obvious from the previous section that the distributions of AE locations observed in the PRT are more consistent with the orientation of Stress Field A rather than Stress Field B if we make the assumption the AEs are primarily controlled by stress. In order to check that AE locations show the same consistency elsewhere in the HRL we have also modelled the excavations associated with the Retrieval Tunnel. The Retrieval Tunnel is at the 420m level close to the ZEDEX volume and hence Stress Field A is assumed to be the correct stress field at this level after *Young et al.*[1996].

Figure 4-13 and Figure 4-14 show the relationship of the observed AEs with induced stresses around the two deposition holes DD0092G01 and DD0086G01 respectively. As in the PRT the AE distributions map regions of excavation-induced compressive stresses suggesting that Stress Field A is consistent with the AE results. This consistency between the PRT and Retrieval experiments also supports the argument that in both cases AEs have been produced through the introduction of increased compressive stresses, probably interacting with regions of weakened (already fractured) rock volumes or changes in lithology as shown from Section 4.1.2. Figure 4-15 shows horizontal sections of the ratio σ_3/σ_1 for deposition holes in both the PRT and Retrieval Tunnel. For the PRT both Stress Fields A and B are shown. In both cases there is very little correlation between variations in this ratio

and the distributions of AEs that have been observed. This provides justification for the assumption that AEs are primarily a result of increased compressive stresses (increased σ_1-σ_3) rather than a result of unloading alone

Figure 4-16 compares the modelled induced σ_3 stresses around the PRT and Retrieval Tunnel excavations using Stress Field A. Low σ_3 stresses are found in zones orthogonal to the high σ_1 zones shown in previous figures. A stress isosurface is shown at σ_3=0MPa. Regions within this isosurface therefore experience tensile stresses. This tensile zone is significantly bigger in the Retrieval Tunnel compared to the PRT, where little or no tensile stresses are observed, although σ_3 does reduce close to 0MPa. This difference must be associated with the different geometries and orientations of the tunnels above. For all the deposition holes monitored, in both the PRT and Retrieval Tunnel, there are very few AEs within these zones. This can be seen by examining Figure 4-3 to Figure 4-6 - in the PRT the tensile zones lie at approximately 60 and 240° from the tunnel axis, and in the Retrieval Tunnel at 120 and 300°. In deposition hole DA3545G01 (Figure 4-3) there are two AE clusters, with small (<20cm) dimensions, occurring in the low σ_3 zone. These may be associated with slip on pre-existing fractures as the normal stress is reduced.

4.2.5 Stress effects from neighbouring deposition holes

AE monitoring in the Retrieval Tunnel showed that AEs were locating around a neighbouring deposition hole whilst excavation of a second deposition hole was being performed. This raised the question whether induced stress concentrations around one deposition hole are being effected by the close proximity (4.25m) of a second deposition hole. If so, what is the stress change experienced around the neighbouring deposition hole? To test this we have utilised a program called DSTRESS that is supplied with the Examine^{3D} package. This software has the facility to subtract one stress model from a second stress model. We have used the excavations in the PRT with stress field A as a case study.

1. We have produced a model with the PRT and deposition hole DA3545G01 excavated.

2. We have then produced a second model with the PRT and both deposition hole DA3551G01 and DA3545G01 excavated.

3. We have subtracted the first model from the second. This gives the difference in stress around DA3545G01 when we have no neighbouring deposition hole to when we have a neighbour fully excavated. Figure 4-17 shows the change in the maximum compressive stress around DA3545G01 from the inclusion of DA3551G01.

Figure 4-17 shows that the stress fields of the two deposition holes are interconnected. Compressive stresses in the direction of the neighbouring deposition hole, along the axis of the tunnel, are increased (or loaded) by approximately 1.5MPa, and are unloaded orthogonal to the direction of the neighbouring deposition hole by a similar amount. This small change in stress concentration may be sufficient to explain the observation that AEs are activated around a first deposition hole by excavating a second close to it. This stress disturbance must then be sufficient to re-activate sliding or extension on existing fractures, or to re-initiate further cracking in the already disturbed rock mass around the neighbouring deposition hole. This could be possible when the rock mass around that deposition hole is already in a highly stressed state as shown in the previous section.

As an extension to this analysis it was of interest to understand what the effect of a third deposition hole would have on DA3545G01. In an operating repository it is proposed that a line of deposition holes will be utilised. In this case, each deposition hole will have two immediate neighbours instead of the one neighbour shown in Figure 4-17. These two neighbours will have a combined effect on the central deposition hole. Figure 4-18 shows the change in the maximum principal stress when a hypothetical third deposition hole, named DA3539G01, is included, compared to the situation when the central deposition hole (DA3545G01) has no neighbours. The effect is to further increase loading in directions along the axis of the tunnel, up to approximately 2.5MPa. Regions orthogonal to this direction are unloaded by approximately 2.5MPa.

The conclusion from this analysis is that, with a spacing of 6m between the collars of neighbouring deposition holes, when a line of deposition holes are excavated in a repository, each will have a stress disturbance effect on its neighbour. This effect was possibly observed as AE activity in the Retrieval Tunnel, although the experiment at that time was not configured to provide any conclusive results. In addition to this it should be noted that many factors contribute to this effect; in particular, the orientation and magnitudes of the far-field stress field and the shape and orientations of the excavations with respect to this. The implication of this is that any repository design will have to be performed accounting for all the excavations that are to be included, as well as the orientation of the far-field stresses and the rock mass behaviour.

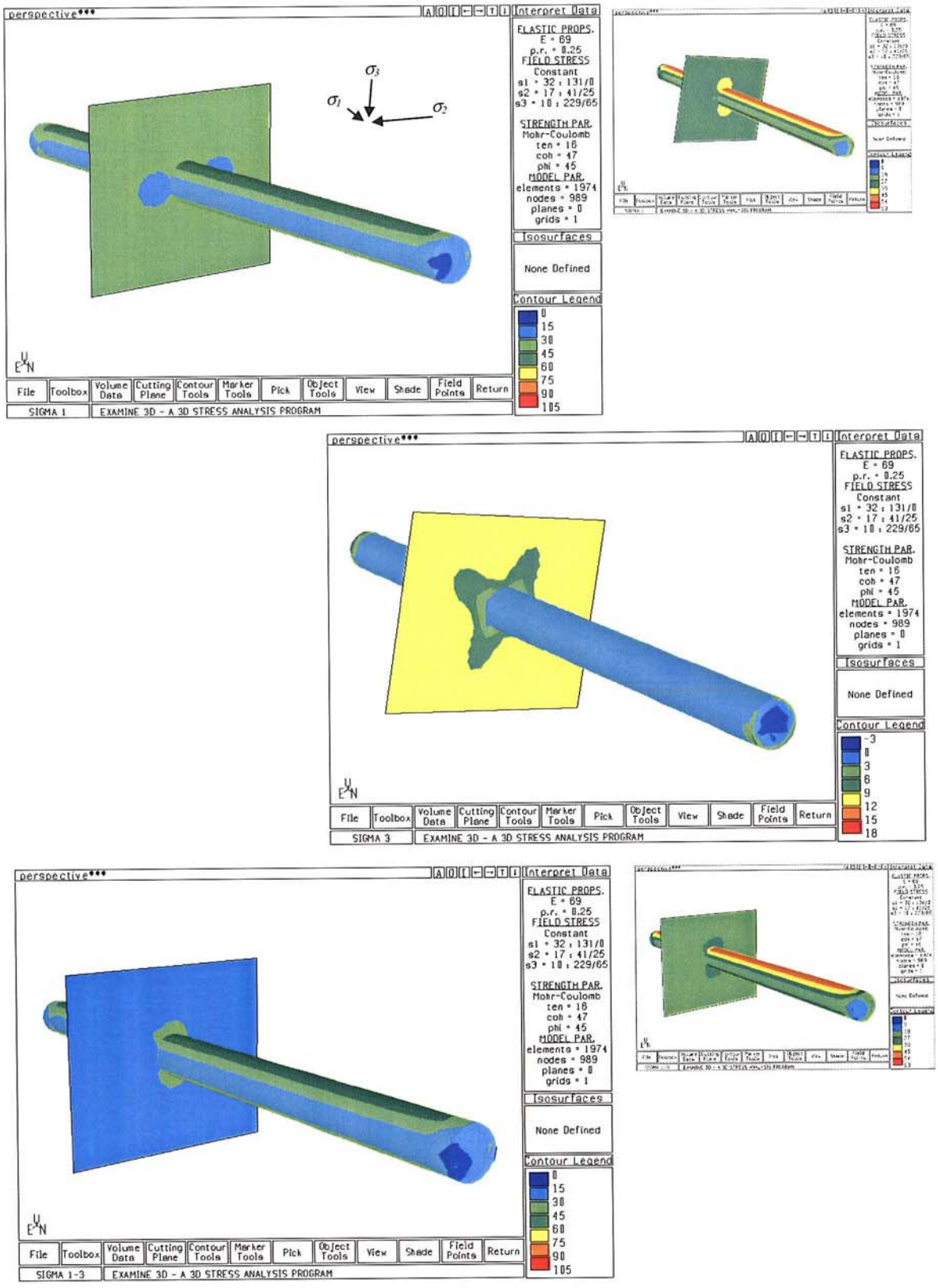

Figure 4-7: Stress analysis of the Prototype Tunnel using stress field A. *The view looks Southeast so that the tunnel end nearest the reader is the face of the tunnel. A vertical cutting plane orientated South to North is shown at 918m East.* ***Top:*** *σ_1 contoured over the tunnel surface and cutting plane (scale has maximum σ_1 of 105MPa for comparison with* ***Figure 4-8*** *- inset plots scale to a maximum σ_1 of 63MPa).* ***Middle:*** *σ_3.* ***Bottom:*** *σ_1-σ_3.*

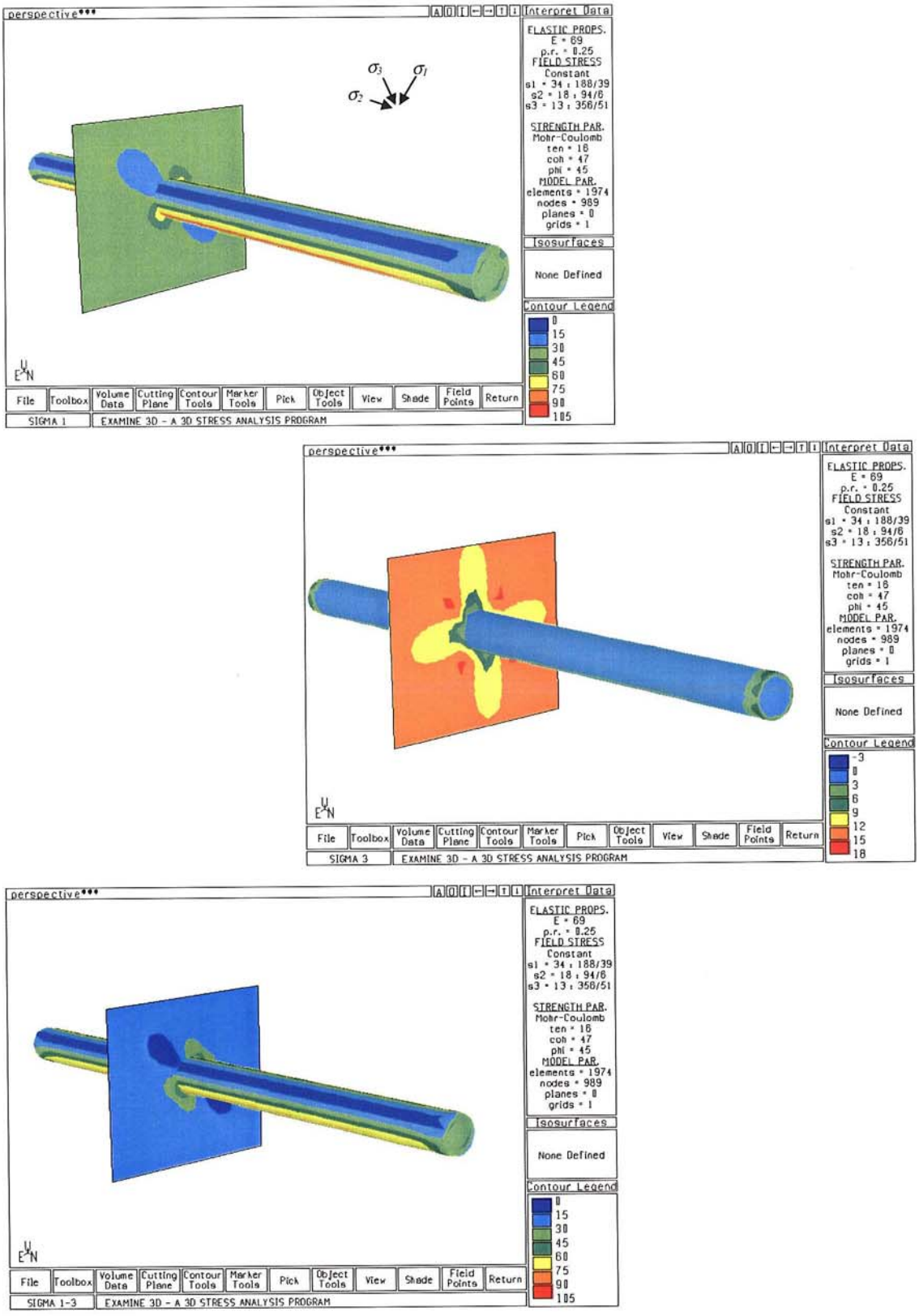

Figure 4-8: Stress analysis of the Prototype Tunnel using stress field B. Top: *σ_1 contoured over the tunnel surface and cutting plane.* ***Middle:*** *σ_3.* ***Bottom:*** *σ_1-σ_3.*

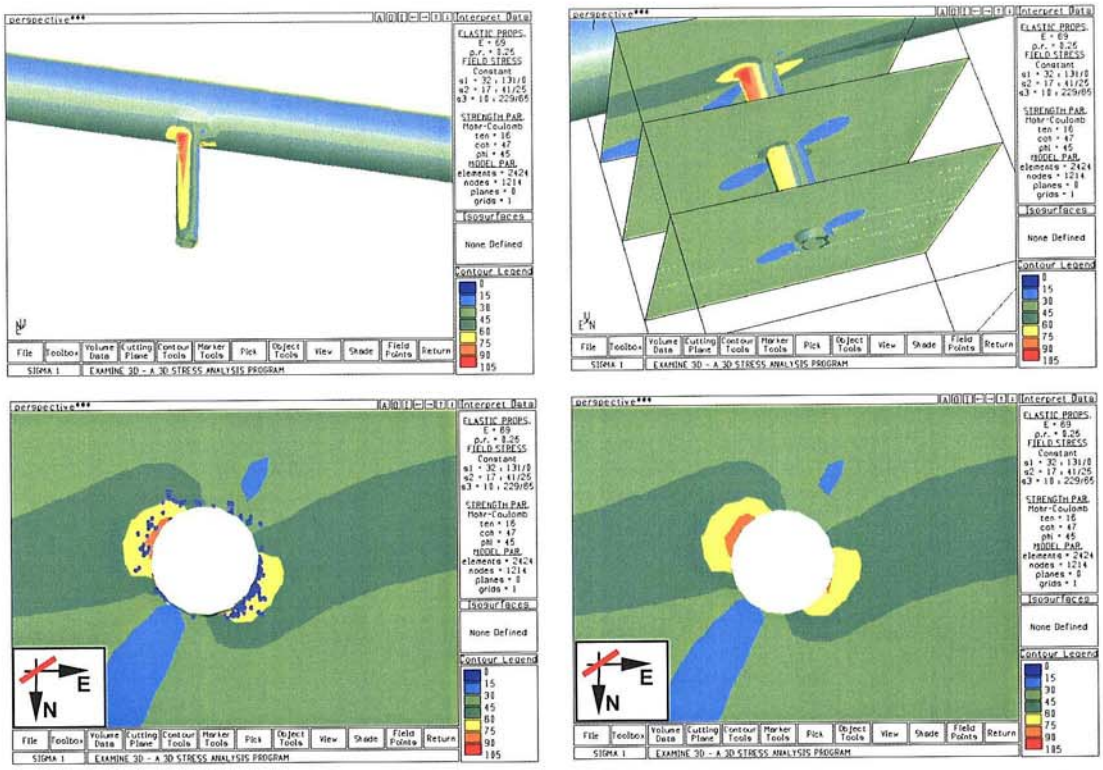

Figure 4-9: Stress analysis of the Prototype Tunnel with a complete excavation of Deposition Hole DA3551G01 in Stress Field A. Upper Left: *Perspective view of the model (induced* σ_1 *is shown).* ***Upper Right:*** *Three horizontal cutting planes through the deposition hole excavation.* ***Lower Left:*** *View onto the upper most cutting plane* from below *with AE locations superimposed (red line indicates far-field* σ_1 *azimuth).* ***Lower Right:*** *As lower left without AE locations.*

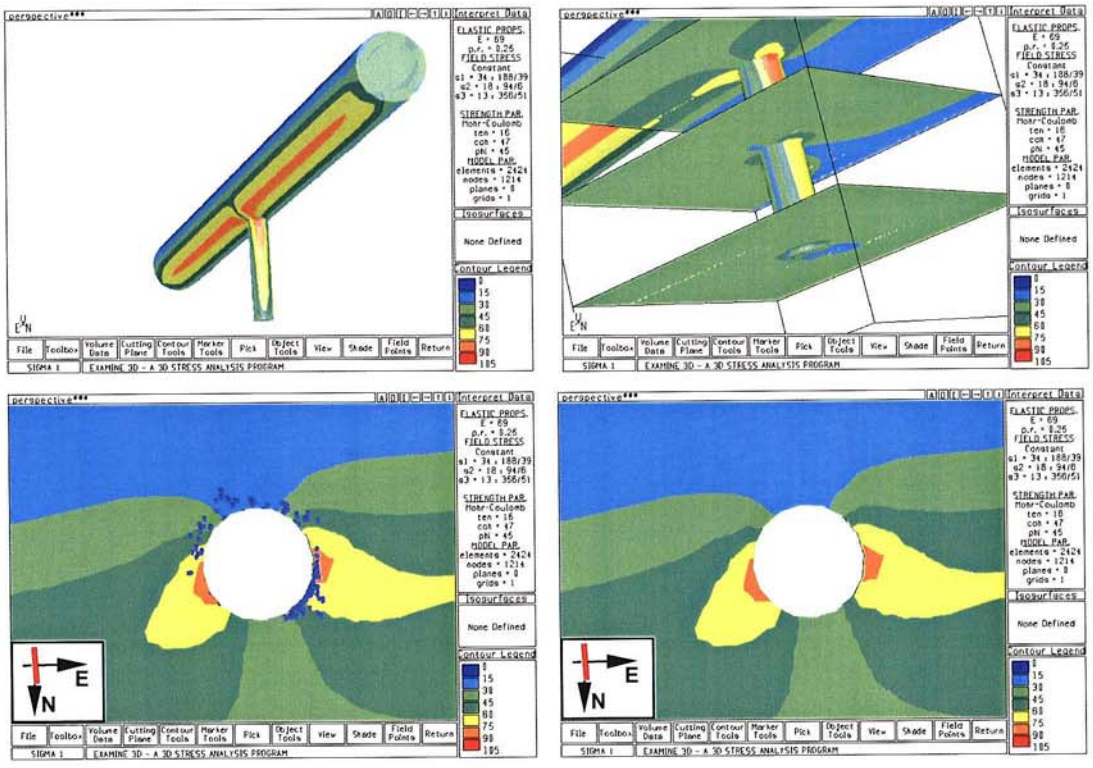

Figure 4-10: Stress analysis of the Prototype Tunnel with a complete excavation of Deposition Hole DA3551G01 in Stress Field B.

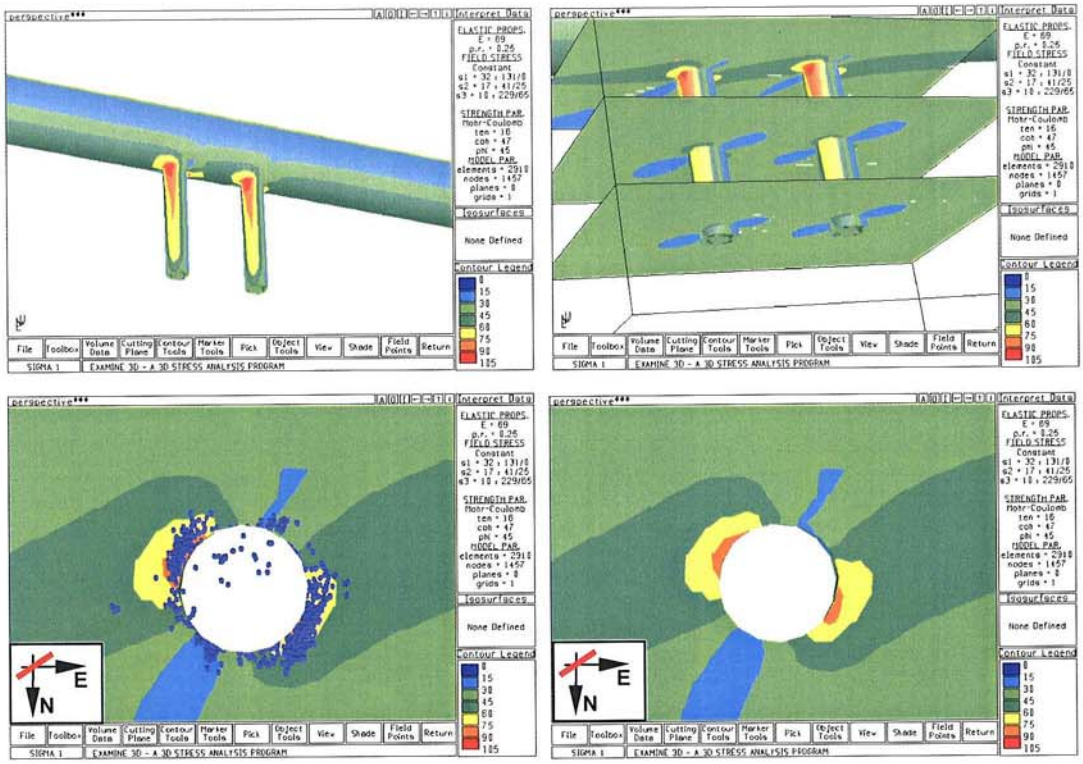

Figure 4-11: Stress analysis of the Prototype Tunnel with a complete excavation of Deposition Holes DA3551G01 and DA3545G01 in Stress Field A. Upper Left: *Perspective view of the model (induced σ_1 is shown).* ***Upper Right:*** *Three horizontal cutting planes through the deposition hole excavations.* ***Lower Left:*** *View onto the upper most cutting plane through DA3545G01 from below with AE locations superimposed (red line indicates far-field σ_1 azimuth).* ***Lower Right:*** *As lower left without AE locations.*

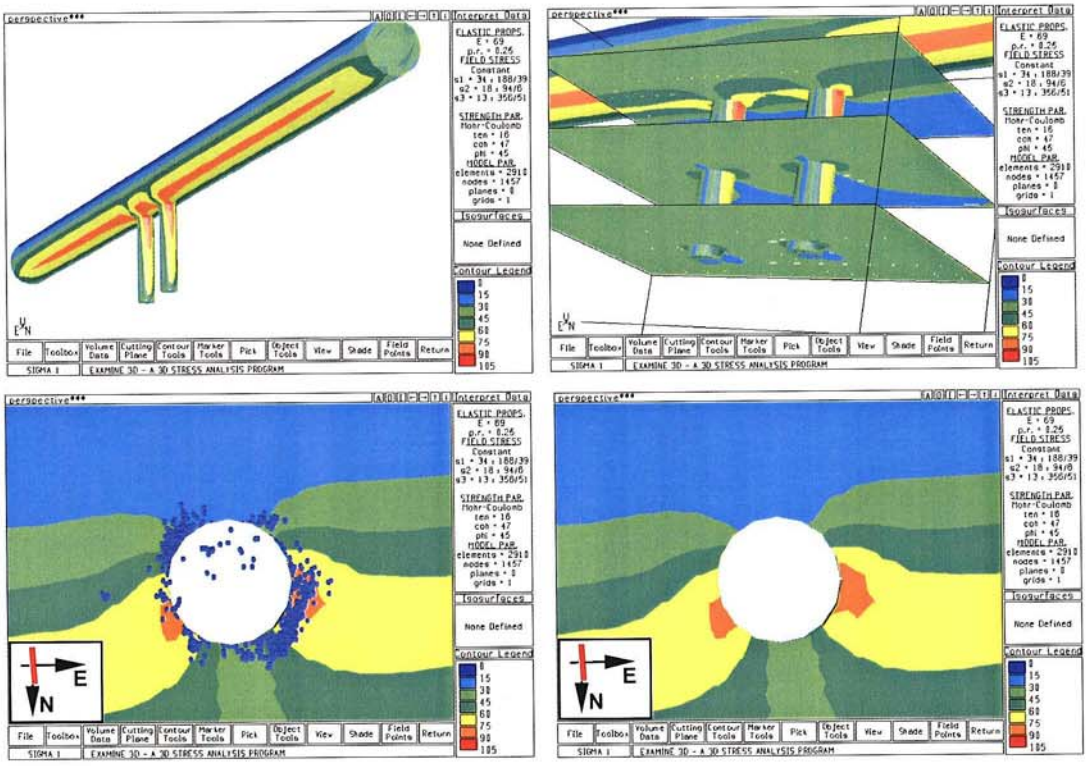

Figure 4-12: Stress analysis of the Prototype Tunnel with a complete excavation of Deposition Holes DA3551G01 and DA3545G01 in Stress Field B.

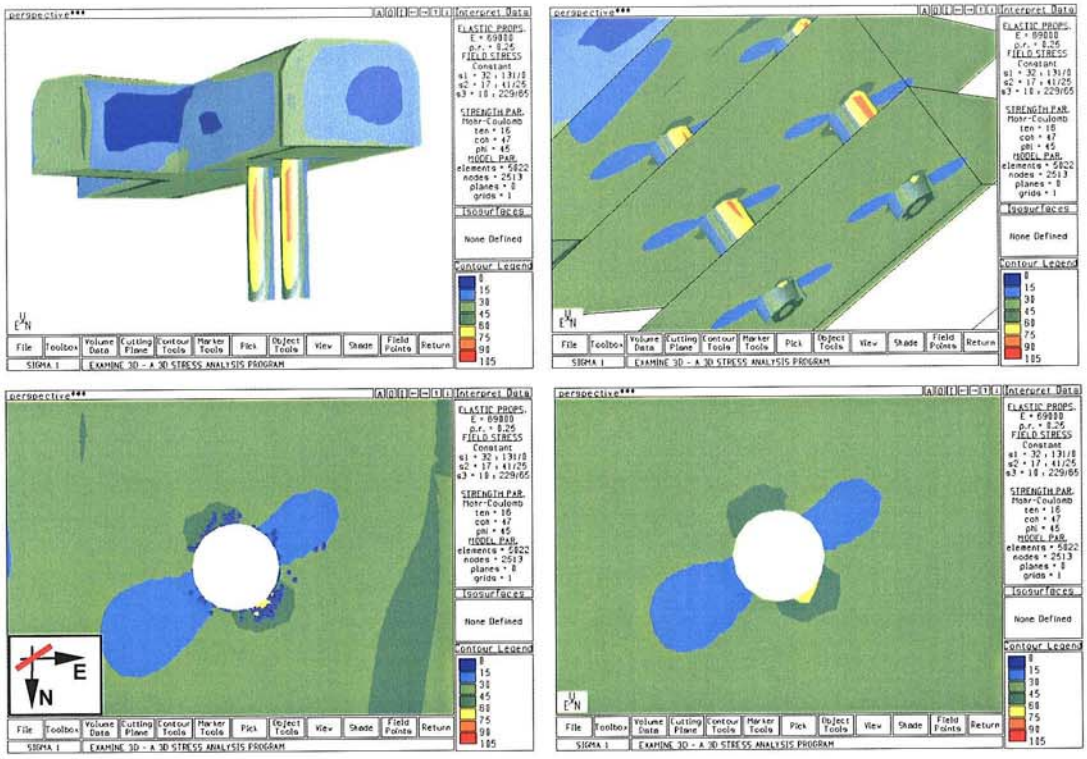

Figure 4-13: Stress analysis of the Retrieval Tunnel with a complete excavation of Deposition Hole DD0092G01 in Stress Field A. Upper Left: *Perspective view of the model (induced σ_1 is shown).* ***Upper Right:*** *Three horizontal cutting planes through the deposition hole excavations.* ***Lower Left:*** *View onto the upper most cutting plane from below with AE locations superimposed (red line indicates far-field σ_1 azimuth).* ***Lower Right:*** *As lower left without AE locations.*

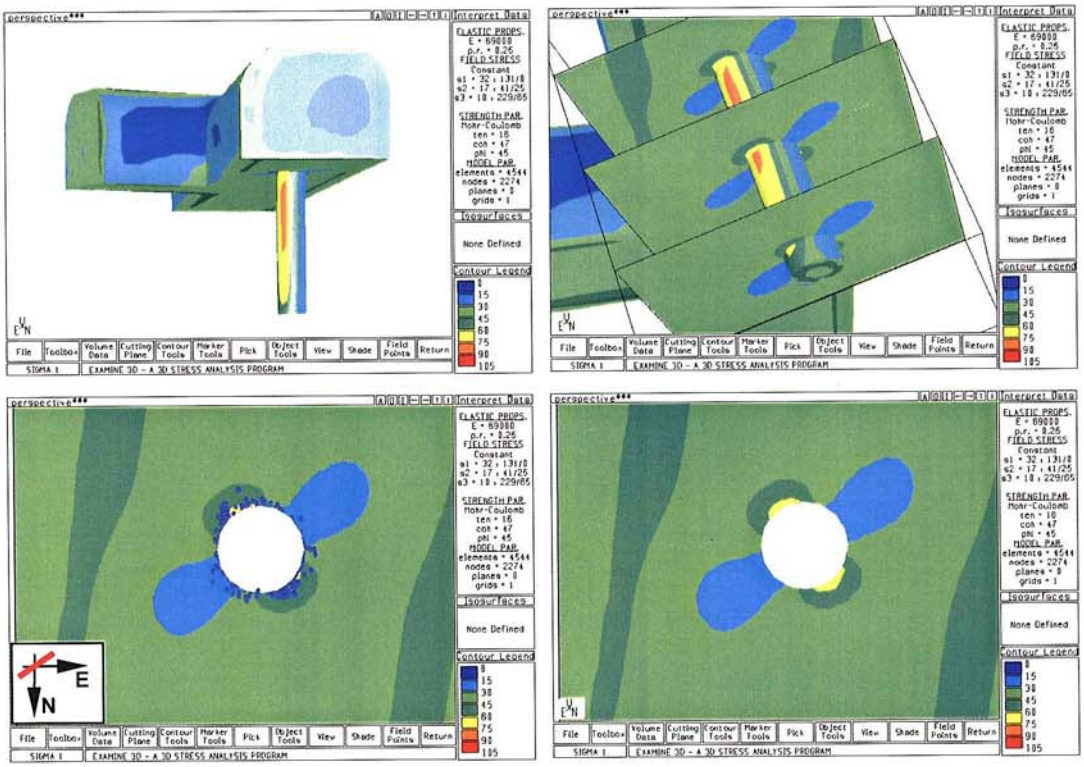

Figure 4-14: Stress analysis of the Retrieval Tunnel with a complete excavation of Deposition Holes DD0092G01 and DD0086G01 in Stress Field A. Lower Plots: *View onto the upper most cutting plane through DA0086G01* from below.

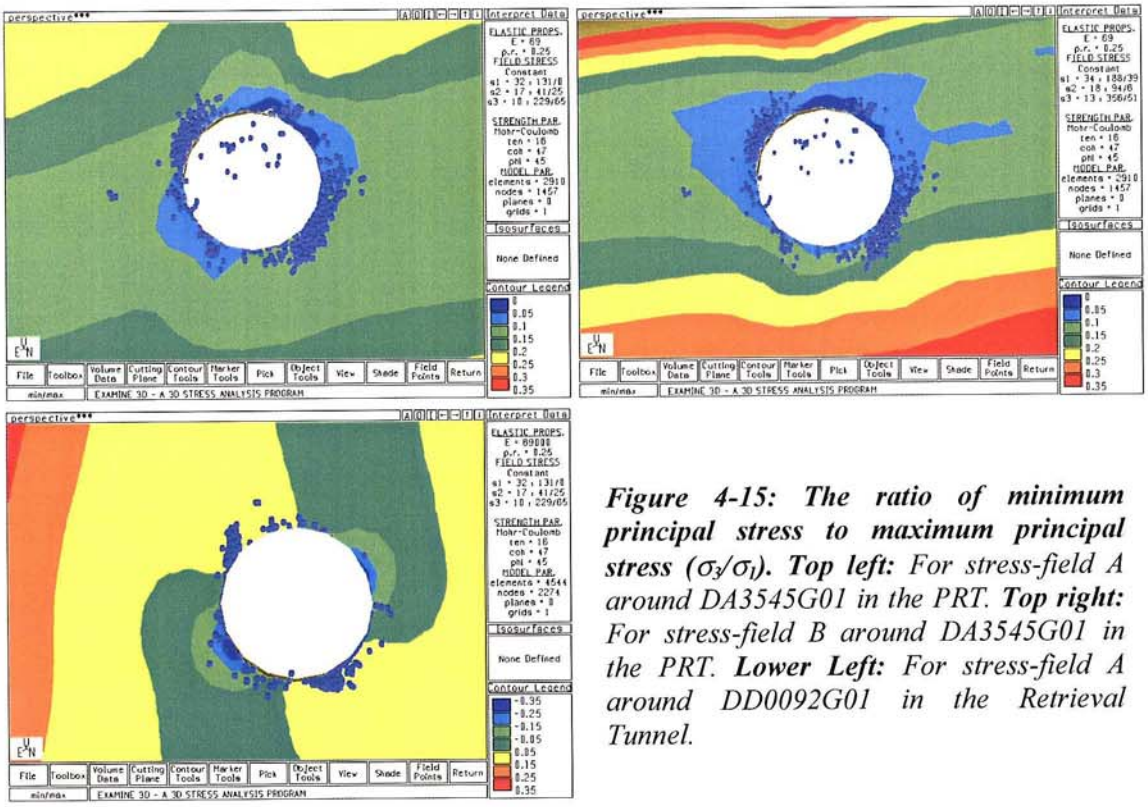

Figure 4-15: The ratio of minimum principal stress to maximum principal stress (σ_3/σ_1). Top left: *For stress-field A around DA3545G01 in the PRT.* ***Top right:*** *For stress-field B around DA3545G01 in the PRT.* ***Lower Left:*** *For stress-field A around DD0092G01 in the Retrieval Tunnel.*

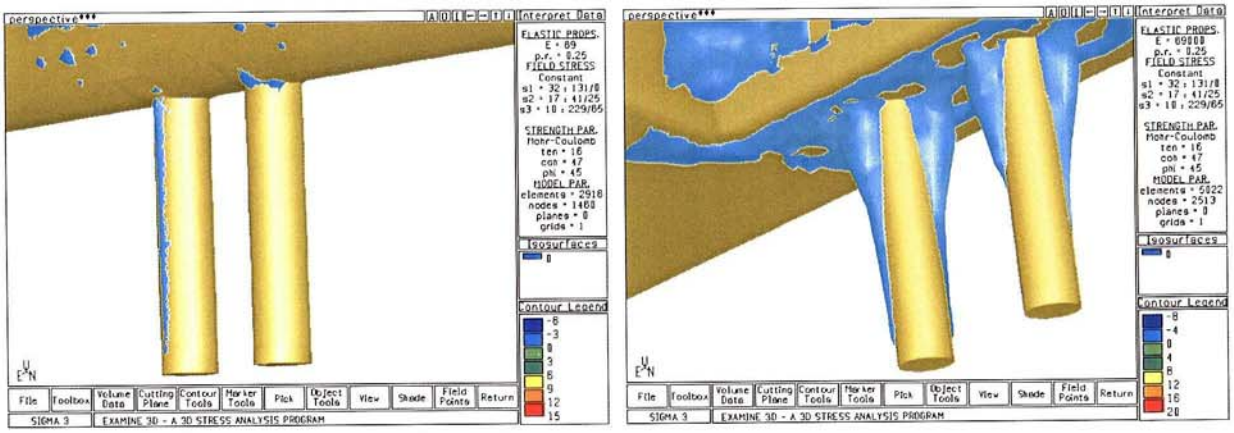

Figure 4-16: Tensile zones associated with deposition holes in the PRT (Left) and Retrieval Tunnel (Right).

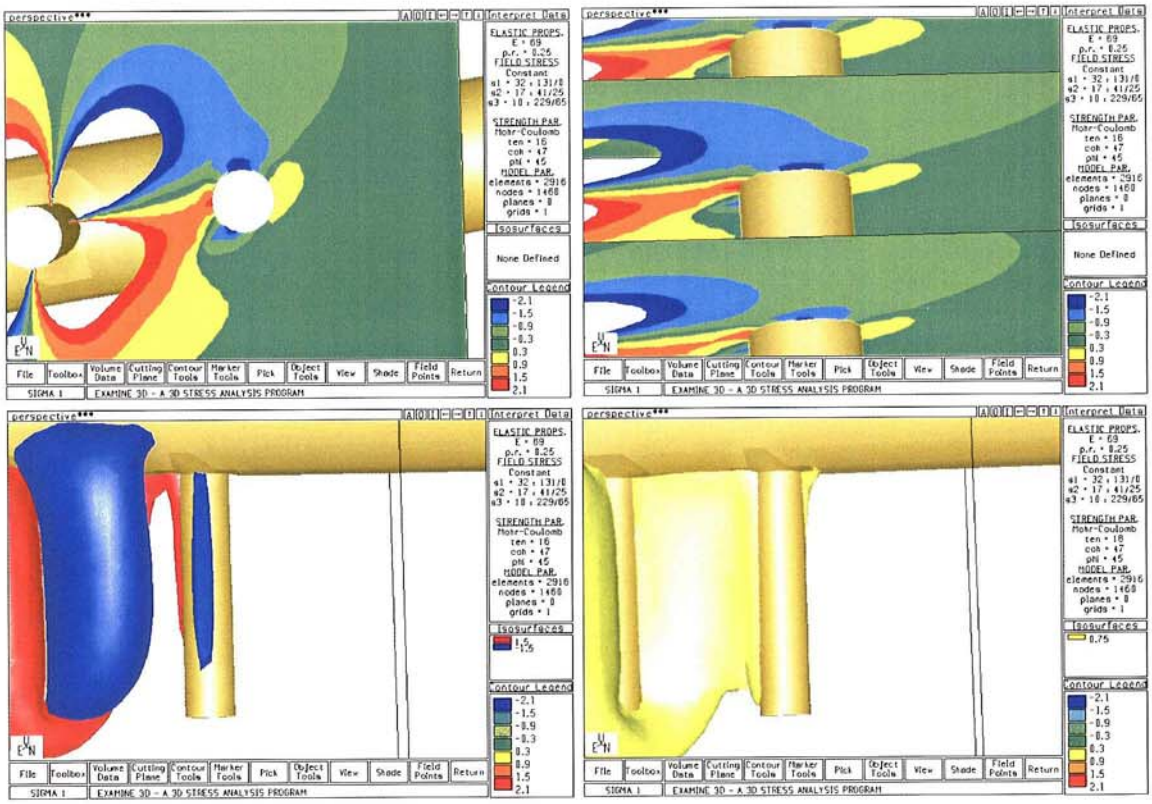

Figure 4-17: The stress disturbance caused by a neighbouring deposition hole using the PRT as a case study. Top Left: *The difference in the maximum principal stress caused by the introduction of a neighbour. A horizontal cutting plane is shown immediately below the tunnel floor.* ***Top Right****: Three horizontal cutting planes down the deposition hole axis.* ***Bottom Left:*** *Stress isosurfaces at +1.5MPa (red) and -1.5MPa (blue).* ***Bottom Right:*** *Stress isosurface at +0.75MPa.*

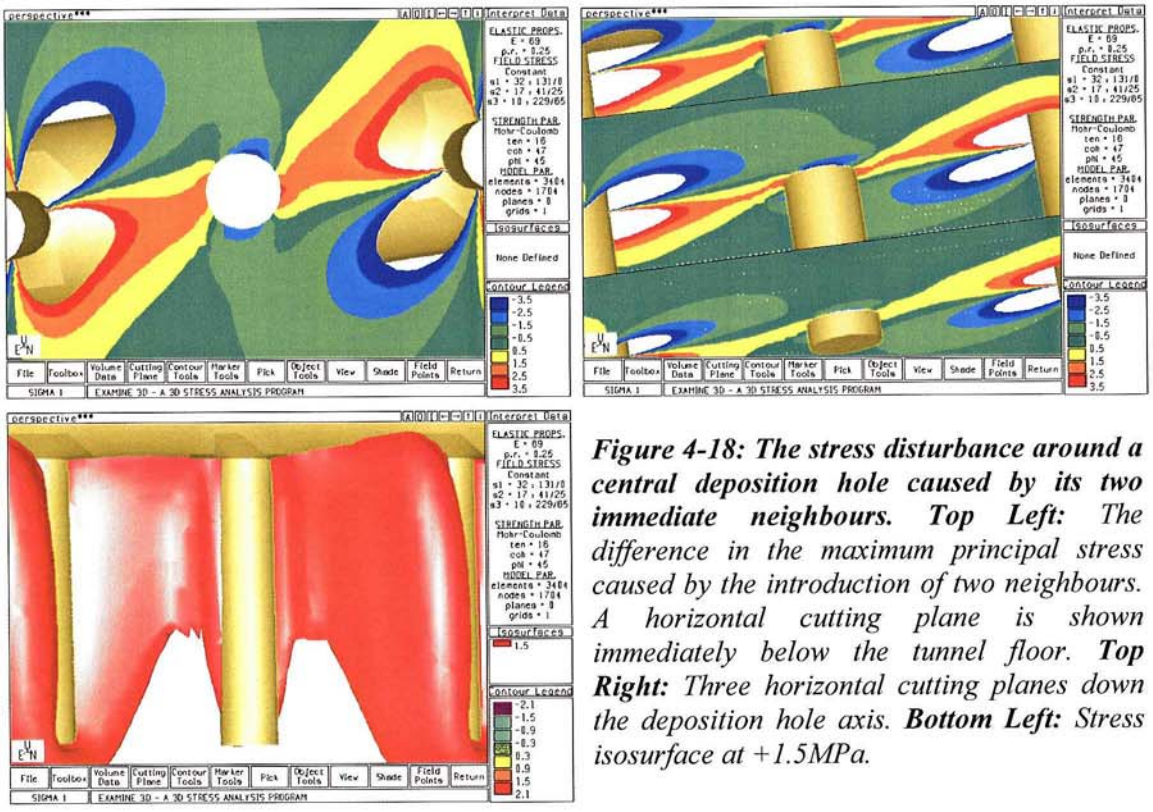

Figure 4-18: The stress disturbance around a central deposition hole caused by its two immediate neighbours. Top Left: *The difference in the maximum principal stress caused by the introduction of two neighbours. A horizontal cutting plane is shown immediately below the tunnel floor.* ***Top Right:*** *Three horizontal cutting planes down the deposition hole axis.* ***Bottom Left:*** *Stress isosurface at +1.5MPa.*

4.3 Objective 3: Discrimination of the stress field orientation using AE source mechanisms

4.3.1 The relationship of seismic source mechanisms to the stress field orientation

A source mechanism describes how failure occurred at the source of a seismic event and is calculated from waveform amplitudes measured over the array of recording sensors. In earthquake seismology the source mechanism is classically depicted using a fault-plane solution representing a shear or double-couple mechanism (e.g. *Gibowicz and Kijko*, 1994). This shows the orientation of the two possible fault planes on which the source occurred and the direction of slip (a slip vector, **s**). Source mechanisms for AEs and microseismic events have been investigated extensively at the URL (e.g. *Feignier and Young*, 1993; *Pettitt*, 1998). Seismicity that occurs at this source scale and in close proximity to voids (excavations) sometimes includes more exotic mechanisms than just a shear (double-couple) model; such as tensile (crack opening) or compressive (crushing), or some complex mixture [*Baker and Young*, 1997; *Pettitt*, 1998]. In this case a moment tensor procedure is used to calculate the source mechanism as it does not assume the source fits a shear model and can resolve these more complex components (e.g. *Gibowicz and Kijko*, 1994). For AEs at the PRT, a similar case to that observed at the URL is likely to exist, with a mixture of events, some with simple shear source mechanisms and some with more complex mechanisms. For the analysis we have conducted here we have used a procedure developed and successfully applied by *Pettitt*[1998] to AEs in laboratory experiments and around excavations at the URL. This procedure is outlined in Appendix A1.

The source mechanism of a seismic event (such as an AE) occurring on a fault plane is related to the principal stress field operating on that plane. The information from the mechanics driving the AEs can therefore be used to back-calculate information on the stress field. There is significant evidence in the literature that the principal axes (pressure, tension and null axes) of seismic source mechanisms are related to the principal stress field. *McKenzie*[1969] shows the relationship between tectonic earthquake mechanisms and measured stress fields. *Collins*[1997] gives examples of the relationship between source-mechanism principal axes and the stress field at the URL. Pressure axes in laboratory experiments have been shown to be orientated parallel to the maximum compressive stress [*Pettitt et al.*, 1998]. *Jaeger and Cook*[1984] (and *Gephart*, 1990) give mathematical relationships between the stress field, a fault plane orientation, and the direction and magnitude of shear stress (and hence likely slip) on that fault plane. We use these relationships to relate source mechanisms obtained from the PRT to the two measured stress fields A and B. In so doing we attempt to determine which of the two stress fields is most compatible with the data.

The relationship between slip on an earthquake and resolved shear stress from the principal stress field has provided methods for inverting for the principal stress field using well-constrained double-couple (shear) source mechanisms over a sufficient number of seismic events [*Gephart and Forsyth*, 1984; *Julien and Cornet*, 1987]. The method of *Gephart and Forsyth* was used by *Urbancic et al.*[1993] in mining-related microseismic data to analyse the stress fields operating in two Canadian mines. In the analysis reported here we attempt to apply the method of *Gephart and Forsyth* to invert for the stress field from the source mechanism data we obtain from the PRT.

In summary, we have used the following outline method to investigate the stress field at the PRT using AE source mechanisms.

1. We have used a moment tensor approach to obtain as many mechanisms as possible from the AE data collected at the PRT. This required us to filter the AEs manually to find those with waveforms suitable for moment tensor inversion. Each of these was then relocated with manual travel-time picks. P-wave amplitudes were picked for each waveform and then inverted for the moment tensor (Appendix A1). Those AEs that did not have sufficient suitable amplitudes, or that gave solutions that were believed to be insufficiently robust, were discarded. The analysis of robustness in the inversion procedure is described in Appendix A1.

2. The quality and abundance of the source mechanism data that we have obtained has then constrained the use of AE source mechanisms in analysing the stress field. It was found that the inversion procedure only worked satisfactorily for AEs located in the floor of each 0.8m

excavation step and then only for excavation steps in the upper half of the deposition hole. This will be explained further in the following section.

3. Using Examine^{3D} we have constructed models for the orientations of induced stresses occurring in the floor of the deposition hole. These induced stresses create the AEs. We then relate the obtained AE source mechanisms to the induced stress orientations from the two measured stress fields A and B. Through this approach we have discriminated which of the two stress fields (A or B) most adequately explains the AE data.

4. Using the moment tensor results we have discriminated between those AEs that fit a dominant shear source model. We have then used the method of *Gephart and Forsyth,* to try and invert for the local stress-field directly.

4.3.2 AE source mechanisms and the stress field orientation in the PRT

Calculation of source mechanisms for AEs in the PRT has been successful for AEs located beneath the floor of each 0.8m excavation step for the first six steps of excavation of deposition hole DA3545G01. This corresponds to excavation of the upper half of the deposition hole down to approximately 4.3m below the tunnel floor. We have obtained solutions for 56 AEs that have dominant double-couple mechanisms. All of these AEs are located within the first few centimetres beneath the floor of the deposition hole. The source mechanisms are shown in Figure A1 in the Appendices. Table A1 gives a table of results for these solutions. These mechanisms have a dominant component of frictional sliding (double-couple), although there are also often significant (>30%) components of isotropic and CLVD decompositions that suggest more complex failure than just simple shear. Hence, some form of additional crack extension component cannot be ruled out from these mechanisms. Due to the ray path coverage problems explained in Appendix A1 we had difficulty in obtaining solutions for AEs located in the side-walls of the deposition hole and in the floor of the deposition hole for excavation steps at greater depths. We were also only able to find a few AEs suitable for moment tensor inversion around deposition hole DA3551G01, due to the much more limited data set obtained from the monitoring. We have therefore restricted the analysis presented here to AEs in the floor of deposition hole DA3545G01.

In order to relate the mechanism results to far-field stress fields A and B, we have modelled the stresses local to the floor of the deposition hole. Figure 4-19 shows stress trajectories for the local stress field beneath the floor of the deposition hole and after Step 1 in the excavation (0.37m depth). Stress models for the excavation after Step 6 show very similar results. There is a clear difference between the two local stress fields. In both cases σ_3 is orientated vertically into the deposition hole void and σ_1 approximately retains its far-field azimuth and lies horizontally. σ_2 is then perpendicular to the σ_1 azimuth and horizontal. For field A, the local σ_1 is at 147°EofN (northwest-southeast), describing the small rotation from the far-field σ_1 (131°EofN) highlighted in Section 4.2.3. For field B, σ_1 is at 8°EofN (north-south) and is exactly parallel to the far-field σ_1. The local stress fields for the two far fields are hence distinguishable beneath the deposition hole floor.

The 56 solutions shown in Figure A1 generally follow a dominant pattern, that is solutions tend to have one nodal plane that is sub-horizontal and one nodal plane that is sub-vertical. The sense of slip is variable with pressure axes (giving the direction of maximum compressive motion on the fracture planes) either orientated around 45° down to the northwest or 45° down to the southeast. Two example solutions of this dominant pattern are shown in Figure 4-20. Figure 4-21 gives a cumulative plot of all the pressure axis orientations.

Sub-horizontal nodal planes are in this case representative of failure on micro-fractures that are sub-parallel to the face of the deposition hole (Figure 4-20). This failure orientation has a normal vector that is orientated vertically, or into the deposition hole volume. The normal vector is hence approximately parallel to the orientation of the local σ_3. Such a failure type was also observed ahead of the excavation face during the Mine-by experiment at the URL [*Collins*, 1997]. Figure 4-22 shows the relationship between shear stress and dip on a hypothetical failure plane beneath the deposition hole floor. The local stress field a few centimetres below the deposition hole floor in stress field A

(from modelling) has approximate stress magnitudes of σ_1=64MPa, σ_2=30MPa, σ_3=3MPa and we use this as a case study. When the failure plane is exactly horizontal (dip=0°) there is no shear stress (τ_s) acting across the plane and the normal stress (σ_n) equals σ_3. When the plane is rotated just off the horizontal both the shear and normal stresses increase. Within the first 20° the shear stress increases much quicker than the normal stress. As the plane approaches a vertical position the shear stress drops off (from a maximum at 45° dip) and the normal stress approaches σ_1. With a sub-horizontal fracture the shear stress is large compared to the normal stress and hence could easily create slip. For a sub-vertical fracture, slip is much less likely to occur as the normal stress is much greater than the shear stress. The likelihood of slip is increased for a sub-horizontal fracture by the fact that σ_3 in the floor approaches zero as the location of the fracture approaches the free surface. There is then the situation that the normal stress on a sub-horizontal fracture approaches zero yet the shear stress acting on it is still significant enough to induce slip.

Figure 4-23 shows the distribution of slip vectors on the nodal planes of Figure A1 that have a dip less than 45° from the horizontal (defined here as 'sub-horizontal'). The slip vectors are distributed with azimuths in the northwest-southeast quadrants and have two conspicuously tight distributions at 100° east of north and 350° east of north on the lower hemisphere, or symmetrically distributed by ±35° from directly northwest-southeast.

The source mechanisms show that the AEs are occurring on micro-fractures that are preferentially orientated sub-horizontal, or sub-parallel to the excavation face. The local σ_1 and local σ_2 are also sub-horizontal (sub-parallel to the plane of the crack) and the local σ_3 is vertical (orthogonal to the plane of the crack). The pressure axes and slip vectors for the source mechanisms are in the northwest-southeast quadrants, so to get a shear stress resolved onto the fracture plane the azimuth of σ_1 must be approximately northwest-southeast. In this case, the slip on the microcracks is then at an acute angle to the σ_1 orientation and is a function of both σ_1 and σ_2 being resolved onto the fracture. This gives the pattern of slip vector orientations shown in Figure 4-23. The source mechanism results are therefore far more consistent with the local stress field having an azimuth of 147°EofN than an azimuth of 8°EofN. Hence, the source mechanism results are consistent with the AE location results of Section 4.2 in distinguishing the far-field stress field A as providing a better correlation than stress field B. Stress field B is again not consistent with the AE results.

The source mechanisms obtained have an ambiguity in their sense of slip; that is the slip vectors (slip of the upper surface of the micro-fracture relative to the lower surface) are sometimes orientated towards the northeast and sometimes towards the southeast. This can be explained by the relative orientations of the fractures and the local stress field. With σ_1 being horizontal and the micro-fractures being sub-horizontal then σ_1 is at a very acute angle to the plane of the fracture. The sense of slip can then be bi-directional with either slip acting towards the southeast, or towards the northwest, depending upon the angle of the fracture plane to σ_1 (Figure 4-20). This is why we observe the two opposing slip directions in the source mechanisms as shown in Figure 4-20. The exact dip and azimuth of a sub-horizontal failure plane in a fault plane solution is poorly resolved as its strike tends to rotate in both azimuth (±180°) and dip (±20°) quite easily. This precludes any further analysis of the relationship between the sense of slip and the fracture plane orientation. It is very easy to envisage the microcracks generating the AEs as very rough surfaces at the scale of the AE source dimension (millimetres), with the microcracks travelling around and between grains. This easily explains any small variations in fracture plane dip that enables slip to occur and in turn causes this bi-directional effect.

Figure 4-24 shows AE locations for solutions with mechanisms that are consistent with the dominant failure type described above. The sense of slip is indicated by the colour of the marker. There is no dependency of the source mechanisms on the locations of the AEs. This is consistent with the argument above; the mechanisms are dependent on small perturbations in the dip of the microcrack and not on where they are located. Also shown in this figure is a stress isosurface at σ_1=55MPa for each of the two stress fields A and B. For A, the local stress field is symmetric resulting in an almost donut shaped region in which σ_1 increases above 55MPa. For B, the local stress field is asymmetric with stresses to the north being greater. The AE locations fit very well into the high stress (>55MPa) zone generated by field A and show no relationship to field B.

4.3.3 Stress inversion for the PRT

We have used the method of *Gephart and Forsyth* to invert the source mechanisms of Figure A1 for the stress field at the PRT. In this case, the method provides a measure of the stress field local to the floor of the deposition hole that can then be related to the modelled stress fields of Figure 4-19. Hence, using the available source mechanism data, it can only provide a discrimination of the two far-field stress fields A and B, and not an absolute measure of the far-field stress field that has been obtained in studies elsewhere. It therefore cannot provide any further information on the stress field than that presented in the previous section, but can provide additional evidence. What we have found is that the method used here on the available source mechanism data does not provide a unique and significantly constrained measure of the stress field that can then be related to the models.

Gephart and Forsyth provide an 'Approximate' and an 'Exact' method of inverting a population of source mechanisms for the stress field. The latter method is much more computationally intensive than the former. In both cases, a grid search is performed over possible orientations of the three principal stresses and the aspect ratio R defined as $(\sigma_2 - \sigma_1)/(\sigma_3 - \sigma_1)$. For each stress model tested in the grid search, shear stresses are resolved onto each of the fault-plane solutions given as an input. In our case, these are the 56 shear-type source mechanisms that have been obtained from the floor of the deposition hole. Assuming that the slip vector must be colinear to the resolved shear stress, then for each fault-plane a minimum rotation is calculated that brings it into an orientation consistent with the stress model. The method also assumes that the principal stress field is uniform across all the events, and discriminates automatically between the two possible fault-planes on the basis of the amount of rotation required in each case. The Approximate method estimates this rotation analytically, whereas the Exact method finds the best solution to the rotation angle through a further grid search. The sum of the rotations across all the source mechanisms gives a misfit at the stress model tested. A search across a grid of possible stress models then yields a misfit space with a minima that provides the best stress model for the available source mechanisms.

In practise, the Approximate method is used to get an estimate of the misfit space. Stress models close to the minima of this space are then re-evaluated using the Exact method in order to get the best possible solution. Using this approach we have used the Approximate method to provide an indication of the orientation of σ_1. We have come across two problems:

1) *Ambiguity in the slip direction.* The source mechanisms have an ambiguity in their slip direction with pressure (and tension) axes preferentially orientated 45° down to the north-west or 45° down to the south-east. This ambiguity has been discussed in the previous section and has been explained by the AEs occurring on sub-horizontal failure planes sub-parallel to σ_1 and σ_2, and orthogonal to σ_3. Failure is allowed to occur because σ_3 (the normal stress on the failure plane) reduces to zero on the free-surface that is the floor of the deposition hole.

2) *Uncertainties in the source mechanisms.* The 56 source mechanisms shown in Figure A1, although having a dominant pattern, have a scatter in their mechanism orientations. This can be seen as the scatter in the pressure axes shown in Figure 4-21. This is due to a number of factors that include: i) uncertainties in the solutions from the moment tensor method; ii) the fact that many of the solutions are not pure shear but in many cases have high proportions of other, more complex, components such as tension; iii) variability in the failure plane orientation from the source scale of the AEs.

The net effect of these two problems is, in this case, a poorly resolved result from the stress inversion method. Figure 4-25 shows the cumulate σ_1-misfit evaluated using the stress inversion. The minimum in the misfit shows the likely orientation of σ_1, and is the summation of misfits at that σ_1 orientation over σ_2 (and hence σ_3) rotated by 360° around σ_1, and the value of R varied between 0 and 1. In this case the sense of slip is ignored and we constrain the inversion to use the horizontal failure planes of the 35 AEs that fit the dominant source mechanism pattern. The method provides two possible minima for the orientation of σ_1. These are orientated around the sub-horizontal and the sub-vertical. The

deepest minima is the sub-vertical orientation. The sub-horizontal minima is very broad and extends around the full 360° azimuth.

The vertical orientation is the σ_3 direction evaluated from the stress models and lies centrally between the two distributions of the pressure axes of Figure 4-21. *Gephart and Forsyth* suggest a correlation between the orientation of σ_1 given by their method and the pressure axis distribution for earthquakes they have tested it on. This correlation has also been shown elsewhere [*Collins*, 1997; *Pettitt et al.*, 1998]. The reason for this relationship is because the maximum shear stress (and hence maximum likelihood of slip) occurs on a fault plane orientated at 45° to the σ_1 orientation (Figure 4-22). For a fault-plane solution, the maximum shear stress on either of the possible failure planes then occurs when σ_1 is parallel to the pressure axis. For the source mechanisms shown in Figure A1 the pressure axes are preferentially orientated in both north-west (NW) and south-east (SE) quadrants of a lower hemisphere, giving two ambiguous distributions associated with slip towards the NW or SE, as described in the previous section. The side-effect of this ambiguity is that the misfit in the method used here smears out over the NW-SE orientation and tends preferentially to the vertical. Our conclusion then is that the stress field is indeterminate using the method of *Gephart and Forsyth* on the available source mechanism data. However, we feel the results described in the previous section are sufficient to discriminate the two measured stress fields and show that the far-field stress-field A most adequately explains the available source mechanism data.

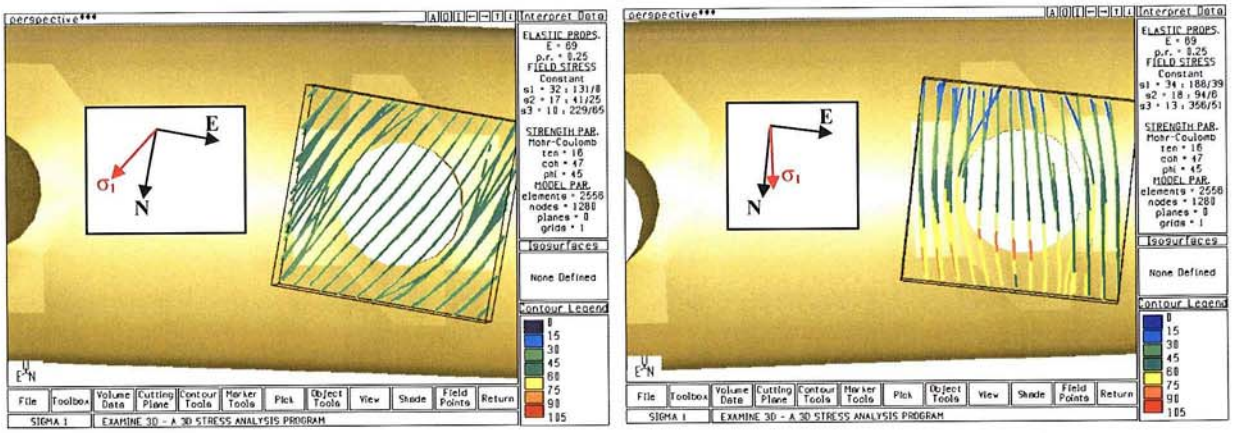

Figure 4-19: Stress trajectory ribbons over the face of deposition hole DA3545G01 after excavation step 1 (0.37m depth). *Left: For stress field A. Right: For stress field B. The view is onto the deposition hole face (vertical and* ***up*** *is into the page). The ribbons have a long axis parallel to the local* σ_1*, a short axis parallel to* σ_2 *and are flat with a surface orthogonal to* σ_3*. In both cases* σ_3 *is into the deposition hole face. The inset box shows the co-ordinate system and the orientation of the local* σ_1 *from the centre of the deposition hole face.*

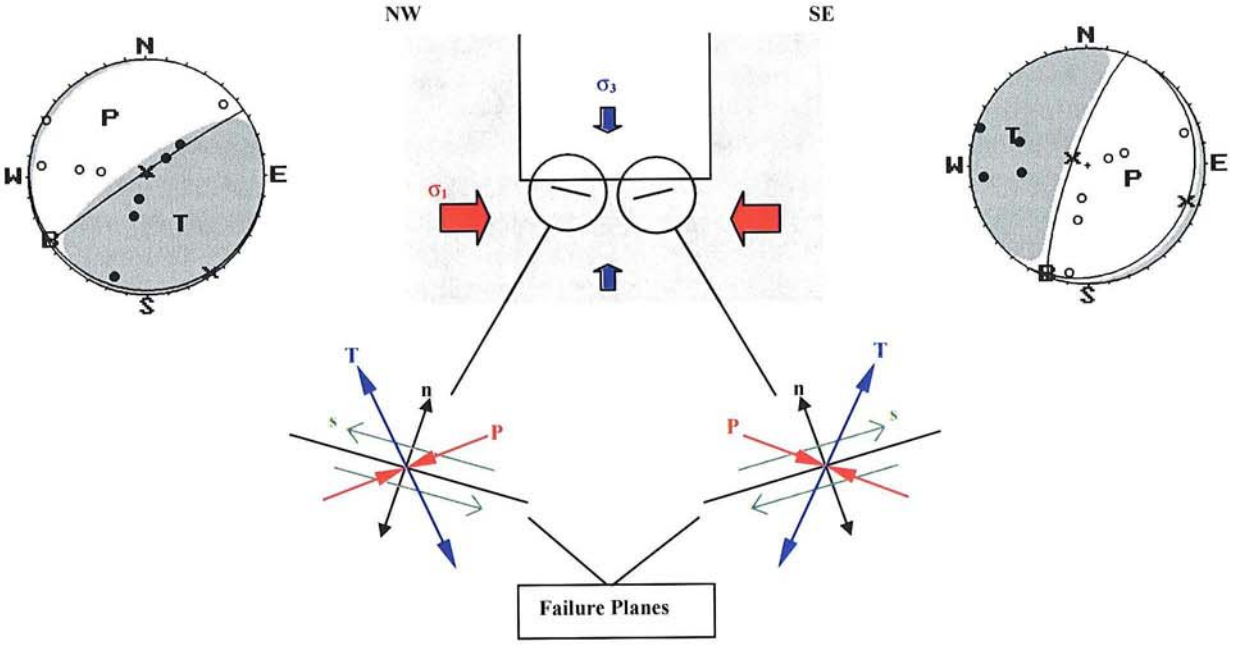

Figure 4-20: Two source mechanisms illustrating the dominant failure type observed in the floor of the deposition hole. Accompanying these are a description of the mechanism orientations with respect to the geometry of the deposition hole and the local stress field. *The plane of the paper is a cross-section through the deposition hole approximately northwest (NW) to southeast (SE).* ***T,P,B*** *correspond to the orientations of the Tensile, Pressure and Null axes respectively. x indicates the orientation of the slip vector,* ***s****, on that failure plane. Filled circles indicate positive first motions. Open circles indicate negative first motions.* ***n*** *is a vector normal to the plane.*

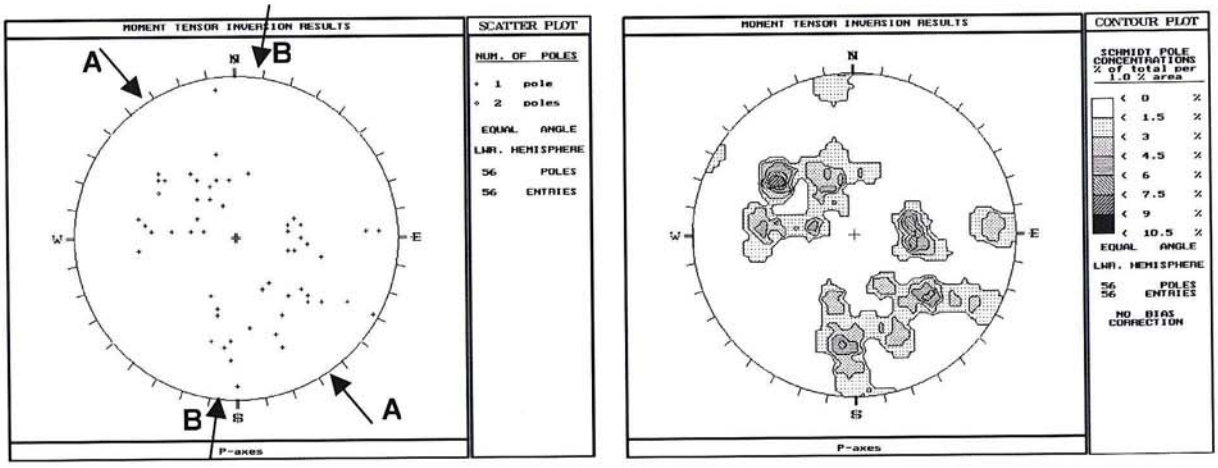

Figure 4-21: Distribution of source mechanism Pressure (P) axes. *Left: scatter plot. Right: Contoured plot. A lower-hemisphere plot is shown. The azimuths of the two measured stress fields are indicated.*

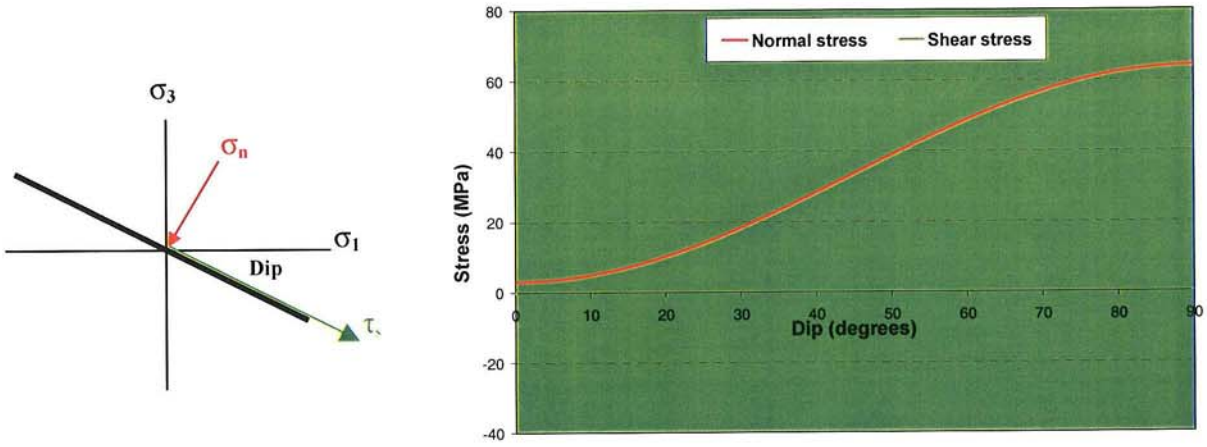

Figure 4-22: Shear and normal stress experienced by a hypothetical fracture beneath the floor of deposition hole DA3545G01 using stress field A. *The fracture is orientated with* σ_2 *in the direction of the fracture's strike (into the page); the* σ_1 *azimuth is then in the down-dip direction;* σ_3 *is vertical. In this case the problem is simplified to a two-dimensional case [*Jaeger and Cook, *1984].* σ_n *is the normal stress on the fracture.* τ_s *is the shear stress.*

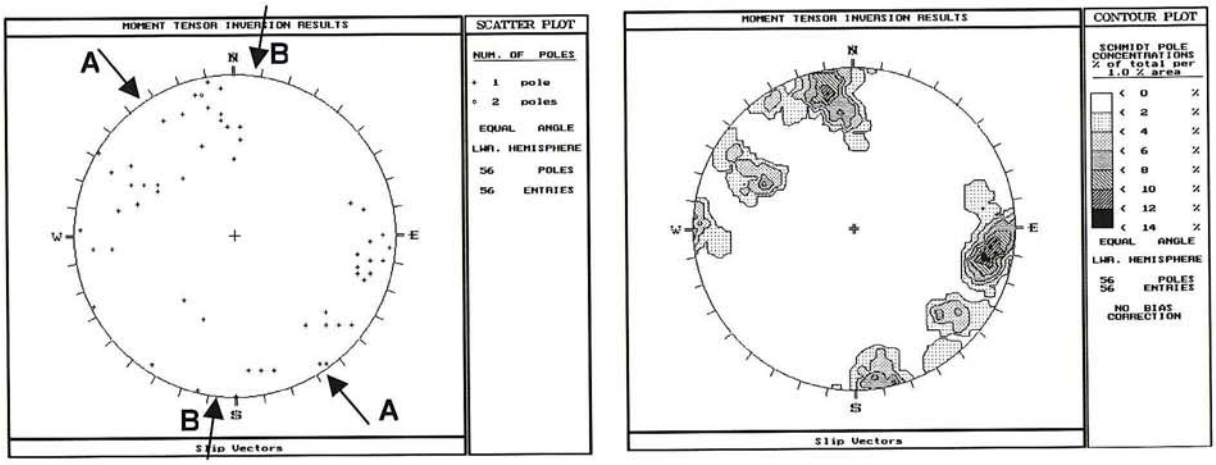

Figure 4-23: Distribution of source mechanism slip vectors, s, on sub-horizontal failure planes (orientated with dips < 45°). *Left: scatter plot. Right: Contoured plot. A lower-hemisphere plot is shown. The azimuths of the two measured stress fields are indicated.*

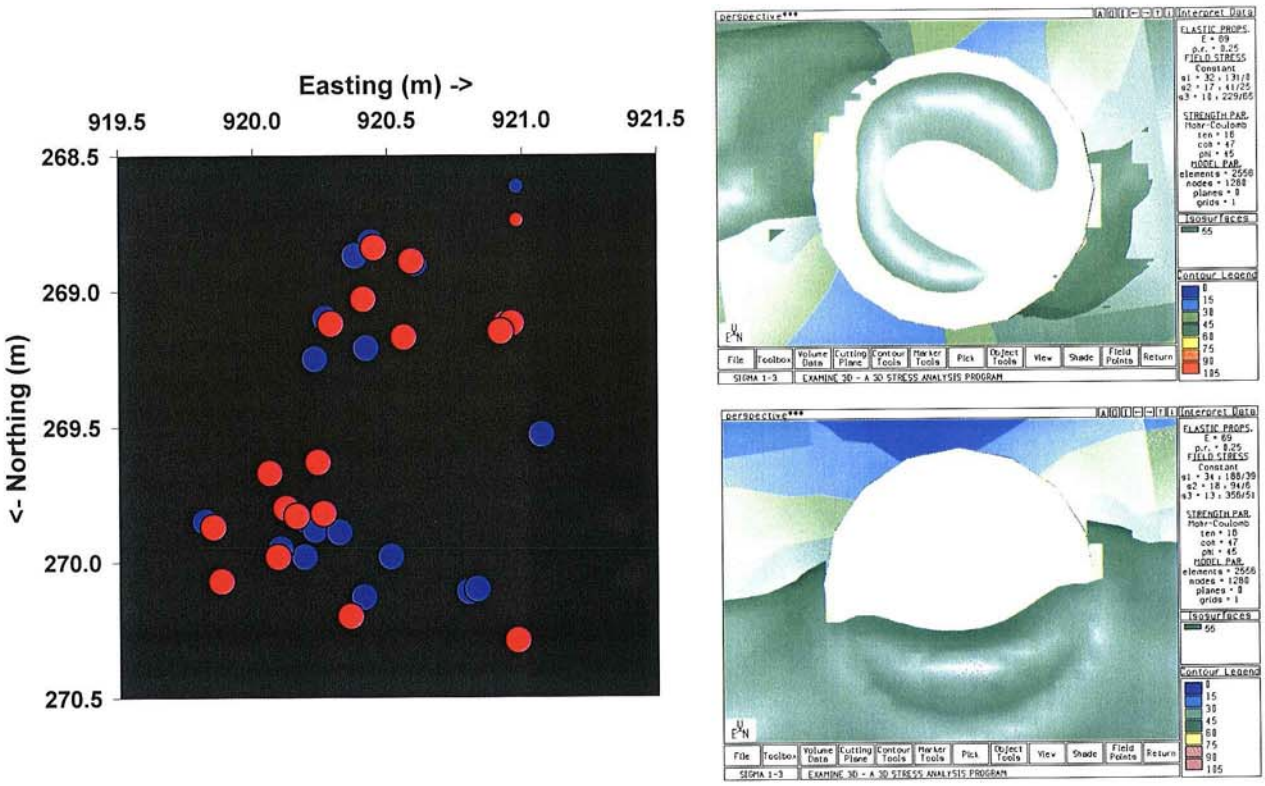

Figure 4-24: Comparison of AE locations in the floor of the deposition hole with modelled stress fields. *Left: AE locations - colour coding indicates sense of slip. Upper Right: The σ_1=55MPa isosurface using far-field stress field A (excavation after step 1). Lower Right: For far-field stress field B. All views are onto the surface of the deposition hole (vertical* ***up*** *is into the page and north is down the page).*

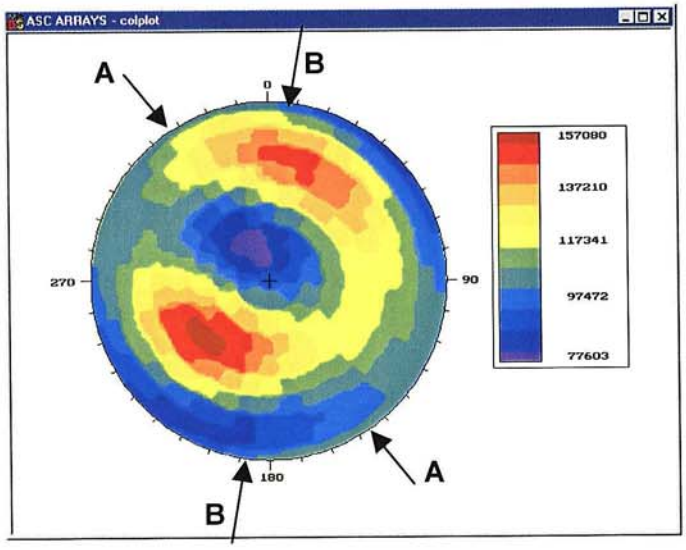

Figure 4-25: Cumulative σ_1-misfit for the stress field at the PRT using the method of Gephart and Forsyth[1984]. *The orientation of the modelled local σ_1 in the floor of the deposition hole is shown for both measured stress fields A and B.*

4.4 Revised results from in situ stress measurements

Since the inception of this project a re-analysis of the stress measurement data from the PRT (labelled 'Measured Stress Field B' - *Table 2-2*) has been conducted elsewhere. Updated principal stress magnitudes and orientations are given in *Table 4-1*, and are an average stress tensor calculated from measurements performed at approximately 470m depth. The updated stress field orientation is shown in Figure 4-26. This is compared with the data compiled by *Leijon*[1995] and the average stress tensor for the 420m level given in *Table 2-1*. The effect of the re-analysis on the measured stress field orientation in the PRT can be seen by comparing the red markers in Figure 4-26 with those in Figure 2-1b. The re-analysis has reported the same stress magnitudes but has brought the principal stress orientations into close agreement with the measurements at the 420m level. However, there is a flip in the σ_2 and σ_3 orientations. This may be due to the fact that these two principal stresses have similar magnitude in this stress field causing the measurements to be ambiguous.

The analysis performed here has compared induced stresses around the PRT excavations, modelled from the two measured stress fields A and B, with AE data. It has been shown that field A explains the observed AE data much more satisfactorily than field B. The re-analysed PRT stress measurements give a σ_1 orientation that is sub-parallel to the orientation of σ_1 in measured stress field A. The σ_1, σ_2 and σ_3 magnitudes are all quite similar for the two stress fields and, although their orientations are reversed, the σ_2 and σ_3 axes have similar orientations. It is therefore likely that if the modelling performed here was repeated with the re-analysed stress measurements then the modelled induced stresses would appear very similar to those from stress field A. The flip in the σ_2 and σ_3 orientations would have a small effect, but this would be reduced as σ_2 is of similar magnitude to σ_3 and both are much smaller than σ_1. For the purposes of this study, stress field A and the re-analysed stress measurements are then equivalent, and therefore the re-analysis of the stress measurement data confirms the results contained in this report.

Stress Component	Magnitude (MPa)	Trend (°)	Plunge (°)
σ_1	34	141	18
σ_2	18	245	80
σ_3	13	50	10

Table 4-1: Re-analysed principal stress values from measurements conducted in the PRT. The results are from a vertical borehole at 470m depth, approximately 20m beneath the tunnel floor.

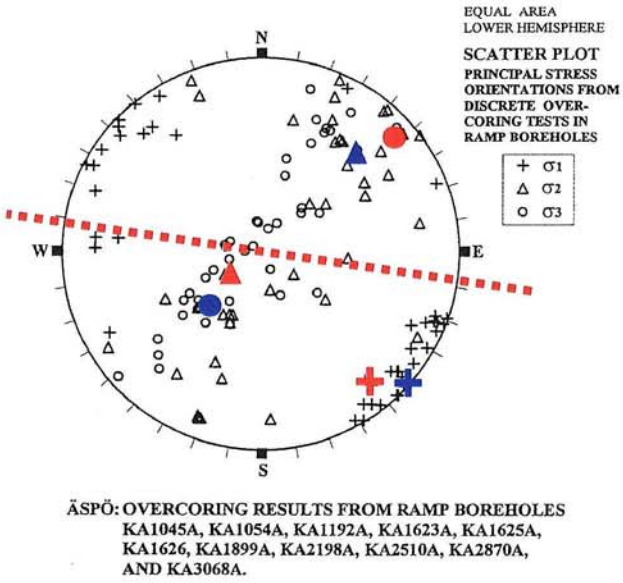

Figure 4-26: Principal stress orientations measured from boreholes excavated from the HRL ramp (black markers) and summarised in Leijon[1995]. *Blue markers are far-field stress measurements A (***Table 2-1***). Red markers are the re-analysed far-field stress measurements from the PRT (***Table 4-1***).*

5 Conclusions

1. Acoustic emission (AE) data have been used to successfully discriminate between two possible measured stress field orientations (described in Section 2) acting in the Prototype Repository Tunnel (PRT). The two measured stress fields have very similar principal stress magnitudes, however their principal stress orientations differ significantly. Each of the stress fields has been used to produce models of induced stresses local to the PRT excavations. The models have then been compared with distributions of AE source locations to test the validity of each. AE source mechanisms have been successfully produced for AEs beneath the floor of excavation steps during the excavation period. The source mechanisms have been related to the two stress field orientations and again used to test their validity. Consistent results from both source locations and mechanisms show that one of the stress field orientations (labelled A) explains the AE data very well, whereas the other stress field orientations (labelled B) has little or no correlation.

2. AE source locations from around deposition holes in both the PRT and the Retrieval Tunnel have been related to geological maps of the deposition holes provided by SKB. AE locations are shown to have a close association with macroscopic fractures. Intense clustering of AEs is produced around fractures in the very close vicinity to the deposition hole wall. In the Retrieval Tunnel a very active cluster is associated with a Pegmatite vein. Not all macroscopic fractures, that have been intersected by the excavation, are disturbed sufficiently to produce AE clustering. Deposition hole DA3545G01 in the PRT is an exception. In this case the deposition hole was very active, relative to the other three monitored, with the vast majority of fractures showing some disturbance. This deposition hole was excavated after its neighbour, DA3551G01. The reason for this difference in AE activity is unclear, although it suggests that the rock mass beneath the PRT is in such a critically stressed state that a small change in the manner of disturbance switches on the AE activity.

3. AE source locations around deposition holes in the PRT have been compared to induced stress distributions modelled local to the excavations. Models have been constructed using both of the tested far-field stress fields (labelled A and B). The two stress fields give very different distributions of induced stresses. The AE locations (in plan) have very tight spatial distributions that are diametrically opposite and suggest a 'breakout' effect, whereby concentrations of induced compressive stresses cause crack initiation to occur, or adjustments on existing microcracks. Induced stresses from field A explain the AE observations very well, whereas induced stresses from field B have little correlation. In order to test that this relationship is consistent across the 420 and 450m levels of the HRL, stress models for the deposition holes in the Retrieval Tunnel have also been produced and compared to AE locations observed there. The same relationship is observed between stress field A and the AE data in the Retrieval Tunnel.

4. The correlation between the observed AE distributions and regions where crack extension would be expected has also been tested by comparing the locations with the spatial variation in the ratio σ_3/σ_1. Previous studies indicate that, for crack extension to occur through unloading, this ratio should reduce below approximately 1.0, although further study is required to thoroughly calibrate this for the Äspö Diorite. In the modelling performed here, there is no spatial correlation between the distribution of AE locations in the side walls of the deposition holes in the PRT, or the Retrieval Tunnel, with this ratio. Instead, there is a very strong correlation between the AE distributions and concentrations of induced compressive stresses, both in the sidewalls and for the examined AEs in the floor of deposition hole DA3545G01. It is therefore concluded that AEs primarily occur around the deposition holes due to induced compressive stresses causing disturbance of pre-existing macroscopic fractures. This disturbance may be related to a combination of new fracture initiation in weakened zones around the fracture, or sliding of pre-existing microcracks in the immediate vicinity of the macroscopic fracture. A relatively small number of AEs occur in modelled low σ_3 zones (these are tensile for deposition holes in the Retrieval Tunnel), and again cluster around macroscopic fractures. These may be due to slip on these fractures as the normal stress on the fracture is reduced.

5. Stress models have been produced that test the disturbance of a neighbouring deposition hole. In the Retrieval Tunnel it was observed that AEs occur around a deposition hole when its neighbour is

being excavated. This suggests that the two deposition holes are introducing a combined disturbance. The stress models show that the induced stress fields of two neighbouring deposition holes are interconnected with a neighbour introducing a loading of 1.5MPa in regions parallel to the tunnel axis and an unloading of 1.5MPa orthogonal to this. By introducing a third deposition hole, as in a repository environment, the effect on the central one is to introduce a further loading/unloading up to 2.5MPa in total.

6. AE source mechanisms have been produced using a moment tensor approach developed specifically for AEs from laboratory and *in situ* experiments. This approach has been used successfully in both laboratory rock testing and at the URL. Mechanisms could only be obtained for AEs located in the floor of excavation steps during the excavation period. This is due to AEs in the side wall of the deposition hole having large numbers of receiver ray paths disrupted by the excavation void. No account for this is taken in the moment tensor method, which assumes a homogeneous isotropic transmission medium. The effect is that accurate and meaningful source mechanisms are very difficult to obtain from AEs in the side wall. We have therefore restricted the analysis to AEs in the floor of the excavation steps and only from deposition hole DA3545G01 (very small numbers of AEs were obtained from monitoring of DA3551G01 resulting in very few mechanisms).

7. The AE source mechanisms show a dominant 'failure' mode. 'Failure', in this case, refers to an adjustment, creation, or extension of a single microcrack in the rock. The dominant failure mode has nodal planes orientated either sub-vertically, or sub-horizontally, with pressure axes orientated into two distributions; one around 45° down to the northwest and one at 45° down to the southeast. There is then a natural ambiguity in the sense of slip of the mechanisms, with failure either to the northwest or to the southeast. It has been shown that these AEs are likely to be occurring on their sub-horizontal nodal planes and hence represent failure on micro-fractures sub-parallel to the face of the deposition hole. The ambiguity in the sense of slip is an artefact of the local σ_1 and σ_2 in the floor of the deposition hole being sub-parallel to the plane of the micro-fracture. Slip directions on the sub-horizontal nodal planes are distributed in the northwest and southeast quadrants of a lower hemisphere and show that the azimuth of σ_1 must be orientated in the northwest-southeast directions. Variations in the slip directions within these quadrants are due to shear stresses resolved onto the fracture plane being a function of both σ_1 and σ_2 (both horizontal). The source mechanism data therefore shows stress-field A to be the more valid stress field of the two measured stress fields considered here. Locations of AEs in the floor of the deposition hole are also more consistent with modelled stresses from stress field A.

8. We have used a method of inverting for the stress field local to the floor of deposition hole DA3545G01 from the available source mechanisms, but have found this data to provide an indeterminate result. This is mainly due to the ambiguity in the sense of slip observed in the mechanisms, but also due to scatter in the source mechanism results. However, we feel that the overwhelming arguments from the correlation of AE source locations and mechanisms with modelled stress fields to be sufficient to discriminate stress-field orientation A, as being the more valid stress field orientation active in the PRT from the two stress field orientations tested. The AE measurements are therefore shown to provide a satisfactory method of validating measured stress field orientations. There is also potential that AEs could be used as a tool to provide a direct measurement of the stress field (both information on magnitudes and orientations), if the monitoring experiment is specifically designed for the purpose of providing large numbers of AEs with well-constrained and spatially diverse source mechanisms. AEs are a response of the rock mass to the induced stress changes resulting from excavation. Therefore when obtaining a measure of the stress field from AEs, the measurement device used to analyse the stress field is the excavation itself. The excavation changes the local stress field around it sufficiently that it induces damage, or disturbance, in the rock mass that is characteristic of the far-field stress field. The advantage of such a technique is that the excavation dimensions (the PRT is 5m in diameter and 100m in length) are many times bigger than small heterogeneities, such as localised fractures, that may disturb the stress field and cause uncertain results from conventional stress measurement devices.

9. The analysis performed in this study has shown that measured stress field orientation A explains all the available AE data (both AE source locations and mechanisms) much more satisfactorily than measured stress field orientation B. A re-analysis of stress measurements from the PRT has been performed elsewhere. This has produced an updated stress field for the PRT that is similar in

magnitude and orientation to stress field A but with a flip in the σ_2 and σ_3 orientations. The results from the re-analysed stress field have therefore confirmed the result obtained in this study, that the AE data is produced by a stress field orientation similar to measured stress field A rather than field B.

6 Recommendations

1) Along with the the work carried out here, ASC propose that it is carried out more work with the objective to construct an *in situ* damage-initiation criterion for 'Aspo Diorite' by modelling induced stresses at the point locations of the AEs. This required a combined analysis of the AE data in stress models, and obtaining laboratory data from triaxial testing experiments. It has become apparent that the experimental component of this work has already been performed by *Nordlund et al.*[1999]. It would be a simple and cost effective extension of the work carried out here to do the work described above using the available AE data and the stress models constructed so far in Examine^{3D}.

2) Research funding should be sought to explore the use of AEs, and other ultrasonic data, to construct a measure of the far-field principal stresses (both magnitudes and orientations) through the use of specifically designed experiments. This may be better performed in a higher stress environment such as at the URL. This could involve an experiment whereby a small-diameter borehole is instrumented in such a fashion as to get very accurate AE locations and, in particular, very accurate source mechanisms, from around the borehole's perimeter (i.e. a miniature deposition hole excavation). Similar experiments could be performed in the laboratory under known stresses in order to calibrate the method. The result would be a feasibility study into whether AEs can be used as a tool to provide precise information on the orientation and magnitude of the principal stresses, and a proposal for how this could be realistically and reproducibly achieved.

7 Appendices

A1: Moment tensor inversion of AE data

A Moment Tensor (MT) inversion has been used to obtain the source mechanisms of the AEs. This approach does not assume a shear (double-couple) type mechanism, but can also resolve more complex mechanisms that might be associated with, for example, opening and closing cracks. It is widely used in mining seismology [*Gibowicz and Kijko*, 1994]. A MT inversion procedure has been developed for AEs recorded in the laboratory and for *in situ* experiments such as that presented here [*Pettitt*, 1998]. The procedure was calibrated in the laboratory, and then used in complex loading experiments [*Pettitt et al.*, 1998, and *Young et al.*, 2000] and at the Tunnel Sealing eXperiment (TSX) at the URL [*Collins et al.*, 2000]. The procedure follows earlier work applied to recordings from lower frequency 'seismic' sensors [*Stump and Johnson*, 1977, *De Natale and Zollo*, 1989, *Feignier and Young*, 1993, and *Ohtsu*, 1991]. The main improvement of the procedure is the consideration of amplitude response functions of the ultrasonic transducers used.

Jost and Herrman[1989] gives a thorough introduction to MT theory and the inversion of seismograms. The method uses amplitude data taken from recorded waveforms and an estimate of the source-receiver propagation effects to invert for the nine equivalent forces at the source. These are represented as a real and symmetric 3x3 matrix, **M**. The MT can then be diagonalised into its three principal forces represented by three eigenvalues and corresponding eigenvectors. The eigenvalues give a measure of the source type (e.g. whether the source is a shear crack or whether it has an isotropic component that might be associated with opening or closing along it). The eigenvectors are the principal axes of the source and, depending upon the magnitude of the corresponding eigenvalue, give the orientations of the pressure, ***p***, null, ***b*** and tension, ***t*** axes. The pressure axis is the direction of maximum compressive motion on the fracture surface and the tension axis is the direction of the maximum tensional motion. The null axis is the vector orthogonal to both the pressure and tension axes and in a double couple solution represents the direction where no motion occurs on the fracture surface. The use of a moment tensor method for AE gives the ability not only to see the location of damage within a rock mass but also the micromechanics that are driving the cracking.

The method for AEs uses P-wave first-motion polarities and amplitudes. These are manually picked from the recorded waveforms. First-break times are also picked and the AE relocated to get more accurate source locations. Assuming a point source and a simple delta type source-time function then a set of recorded amplitudes can be related to the nine equivalent forces at the source by the linear Equation A1, where **u** is a column vector containing the n recorded amplitudes, **G** is a nx6 matrix containing the Green's functions components and **m** is a column vector containing the six required MT elements (only six are required due to tensor symmetry).

$$\mathbf{u} = \mathbf{G}\mathbf{m} \qquad \textbf{(Equation A1)}$$

The Green's functions take into consideration the radiation pattern of the source, the propagation effects along the path and the receiver's response effects. We simplify these by assuming that the receivers are in the far-field (usually estimated as 10 wavelengths) and that the propagation medium is homogeneous and isotropic. Because of the uniaxial nature of the transducers we are restricted to using P-wave amplitudes from the time domain. **G** then contains the P-wave radiation components which can easily be calculated from the known locations of the AE source and receiver (e.g. *De Netale and Zollo*, 1989). Because of the frequency bandwidth and element diameter of the transducers used in this experiment they can be treated as point receivers. They then have no frequency dependent azimuthal effects that are associated with larger diameter, higher frequency, piezoelectric transducers.

Knowing the source-receiver path length, *r*, each amplitude in the vector **u** is first corrected for path and sensor effects including geometrical spreading, anelastic attenuation, free-surface amplification at the transducer face and receiver coupling. The latter is an estimate of the sensitivity of a particular transducer depending upon how efficiently it is coupled to the rock surface. This is estimated from P-

wave amplitudes determined from the three-dimensional ultrasonic surveys. For calculation of anelastic attenuation, a typical estimate of the P-wave quality factor for granite, Q=200 has been used. Anelastic attenuation and free-surface amplification corrections use mean P- and S-wave velocities calculated from ultrasonic surveys conducted during the experiment. The free-surface amplification correction also considers the uniaxial nature of the sensors. The matrix **G** can then be inverted using Singular Value Decomposition (e.g. *Stump and Johnson*, 1977) and the vector **m** subsequently calculated. The six elements of **m** are then used to fill the real and symmetric 3x3 MT matrix, **M**.

Two software algorithms have been produced to enable inversion for the MT. PICKER provides waveform visualisation and algorithms to pick the amplitudes needed. WIMTIP provides the inversion of the amplitudes to give the MT, and then decomposition of this to provide an analysis of the type and orientation of the source mechanism. This is traditionally plotted on a focal sphere (lower-hemisphere plot). WIMTIP also provides a quality assessment of the inversion. In practise, the 16 waveforms recorded for each AE are manually picked for arrival times. The AE is then located using these arrival times to give as accurate a location as possible. It is then re-processed, picking amplitudes for the inversion and performing the inversion itself. The amplitudes are generally picked depending upon how much confidence the user has in the amplitudes; it is sometimes difficult to infer the true first motion from the noise. Amplitudes that have a high confidence are used first to provide a first pass of the inversion. Amplitudes that have less confidence are then included to constrain the mechanism as much as possible. Solutions using a greater number of arrivals (generally >8) distributed evenly over the lower-hemisphere (good focal-sphere coverage) have the most robust results.

Two problems are encountered when using this approach for AEs at the PRT:

1) The array geometry was designed to enable good AE locations around the complete deposition hole perimeter, and to conduct three-dimensional velocity surveys along ray paths passing close to the deposition hole wall. It has not been designed with AE source mechanisms in mind. The problem with the array geometry is that the array is small in relation to the deposition hole size, and the sensors are positioned down four linear boreholes. This causes AEs that occur around the side walls of the deposition hole to be close to the edge of the array, resulting in the focal-coverage being sometimes poor for these AEs.

2) The inversion procedure assumes direct ray paths between the AE source and the receiver, and considers the rock mass as a homogeneous, isotropic medium. It therefore ignores complexities such as major changes in lithology, the effect of fractures on the transmission, and the effect of the excavation void. The excavation void is the most serious problem encountered. When the excavation lies between the AE source and the receiver the energy has to propagate around the void. This produces a serious disturbance to the recorded signal. The result is that any solution that uses these amplitudes generally results in high uncertainties. Amplitudes that encounter this problem therefore cannot be used. This effect is most serious for AEs located in the side-wall of the deposition hole, as usually one or two monitoring boreholes (8 sensors) are effected. AEs located in the deposition hole floor can only use ray paths transmitted downwards, so these are also effected for excavation steps at depths greater than 4m (there are then 8 sensors above the level of the floor).

An important consideration when performing an MT inversion is the quality of the solution. A higher quality solution will be more robust and have less uncertainties associated with it. A series of parameters are provided to try to quantify the quality of the solution.

a) **Amplitude Residuals.** The MT is used to produce amplitudes expected at the array of receivers. These are compared to the actual amplitudes recorded; the difference between the two being the amplitude residual. Amplitudes that have a residual of >0.2 are generally checked and either re-picked or discarded from the inversion. A final RMS amplitude residual is produced from all those used in the inversion to describe the overall fit of the solution to the data.

b) **Error Factors.** Estimated uncertainties in the amplitude measurements are compared to the amplitude residuals from the inversion. Amplitudes that have residuals much greater than would be expected from the uncertainties (Error Factor >> 1) have to be re-assessed. Nodal or small amplitudes

often produce very large Error Factors that are just an artefact of a small amplitude being used in the inversion. An RMS error Factor is produced for the final solution.

c) **Quality Index.** The 6x6 co-variance matrix of the inversion is obtained. This assesses the quality of the inversion of the Green's functions matrix, **G** and so does not consider the amplitude data. A poor inversion is often produced when receivers have a poor focal coverage. In these cases elements in the co-variance matrix become large. In order to reduce this down to one number the quality index is defined as the sum of the squares of the co-variance elements and is hence a warning of a poor inversion.

d) **Condition number.** The condition number allows a qualitative assessment of the robustness of the inverse method (how well it can tolerate a few bad data). Generally, condition numbers of a few tenths to a few units indicate a very robust inversion.

A2: Source mechanism results in the PRT

Table A1: Results for 56 AEs located in the floor of deposition hole from the upper six excavation steps. *These mechanisms are those obtained with a dominant double-couple solution. Columns from left to right (greater explanation for parameters used can be found in Appendix A1): Date and Time of the AE; number (n) of amplitudes used to produce the solution; percentage isotropic, double-couple and CLVD components; Strike, Dip and Rake of the two fault planes; Mean signal:noise (S:N) ratio of the amplitudes used; mean RMS residual on amplitudes; factor of mean RMS residual to estimated errors; quality factor (q) of inversion; condition number (C) of inversion.*

Date	Time	n	%ISO	%DC	%Clvd	Strike1	Dip1	Rake1	Strike2	Dip2	Rake2	S:N	RMS	*Error	q-factor	C
Step #1																
14/09/1999	9:58:01	8	10	-89	-1	284	89	122	16	32	2	17.4	0.10	1.3	20.3	5.4
14/09/1999	10:00:04	10	8	56	36	188	9	-26	303	86	-98	8.6	0.18	1.1	8.6	4.5
14/09/1999	10:00:54	8	-11	-71	-18	218	86	69	117	21	168	5.5	0.14	1.7	12.3	5.3
14/09/1999	10:07:25	9	29	46	25	334	89	-46	65	44	-179	7.7	0.11	0.3	8.5	5.2
14/09/1999	11:29:23	11	-24	66	10	259	35	150	14	73	58	11.0	0.11	0.6	7.6	5.3
14/09/1999	11:43:41	9	-45	-55	0	29	81	79	260	14	140	14.7	0.07	0.7	115.0	8.3
14/09/1999	15:08:00	11	33	38	29	168	77	62	56	31	154	4.6	0.10	1.1	22.6	4.7
14/09/1999	15:08:38	10	-15	-72	-13	29	11	-81	200	79	-92	9.4	0.14	1.9	3.0	2.9
14/09/1999	15:09:01	10	18	53	29	97	4	131	236	87	88	5.7	0.15	4.7	4.6	4.2
14/09/1999	15:11:29	10	-29	-47	-24	70	22	-37	195	77	-108	6.9	0.13	3.1	3.8	2.9
14/09/1999	15:15:32	14	32	48	20	272	20	89	93	70	90	11.0	0.11	2.5	3.7	3.6
14/09/1999	15:39:00	12	4	76	20	16	19	121	164	74	80	7.4	0.09	1.2	5.3	3.5
14/09/1999	15:41:29	11	-9	-78	-13	185	81	92	354	9	80	9.8	0.15	5.8	5.2	3.9
14/09/1999	15:43:42	12	-29	52	19	191	86	-99	76	10	-25	14.5	0.14	1.6	2.9	4.4
14/09/1999	15:43:48	10	-39	-54	-7	71	20	-19	180	84	-109	14.0	0.07	1.0	7.4	4.1
14/09/1999	16:12:29	12	-24	-60	-17	298	22	177	31	89	68	7.8	0.10	0.9	3.9	4.6
14/09/1999	16:15:39	11	-18	-51	-31	79	83	-102	317	14	-32	6.0	0.21	2.5	4.4	3.4
Step #2																
14/09/1999	17:19:36	7	14	48	37	82	28	150	199	76	65	6.1	0.00	0.0	4.0	2.7
14/09/1999	17:19:49	13	32	-43	-25	49	52	118	189	46	59	5.1	0.10	1.0	8.4	4.1
14/09/1999	17:19:51	9	26	-51	-24	221	78	-120	112	32	-23	6.9	0.13	1.2	719.0	17.5
14/09/1999	17:20:20	10	-27	-47	-25	329	39	-34	87	69	-124	6.2	0.16	2.6	1.5	2.2
14/09/1999	17:21:10	12	18	-45	-37	196	81	70	82	22	155	9.3	0.14	1.8	1.0	2.5
14/09/1999	17:35:02	11	4	-79	-17	193	80	70	77	22	153	13.9	0.13	3.7	1.2	2.5
14/09/1999	17:45:26	14	-33	-52	-15	85	47	-123	308	52	-60	794.0	0.10	1.6	51.6	7.3
14/09/1999	17:48:12	11	-19	70	11	272	30	88	94	60	91	15.6	0.13	0.9	135.0	10.7
14/09/1999	18:47:03	8	2	63	35	171	38	8	75	85	128	15.7	0.12	8.3	2.4	3.0
Step #3																
15/09/1999	10:21:48	8	-5	-94	-1	249	21	162	355	84	70	10.1	0.10	1.7	17.7	7.5
15/09/1999	10:21:58	9	11	-78	-12	271	38	90	92	52	90	7.7	0.13	1.6	86.7	7.0
15/09/1999	10:21:58	8	-4	-87	-9	210	16	54	67	77	100	15.6	0.12	0.9	191.0	11.6
15/09/1999	10:47:19	7	-5	-62	-32	34	62	-73	182	33	-118	7.6	0.02	0.0	408.0	13.5
15/09/1999	13:48:32	9	39	53	8	164	77	-8	255	82	-167	12.1	0.13	0.8	86.2	14.1
15/09/1999	14:00:00	7	-29	40	31	144	42	42	20	63	123	10.1	0.06	0.1	34.8	9.9
Step #4																
15/09/1999	15:28:49	8	-29	-49	-22	154	28	-137	25	71	-69	6.6	0.11	3.9	44.9	5.9
15/09/1999	15:28:49	7	16	-78	-6	141	53	32	30	65	139	5.6	0.04	0.1	1350.0	18.0
15/09/1999	15:28:52	8	19	-75	-6	126	49	-26	234	71	-136	7.9	0.07	0.1	21.0	8.3
15/09/1999	15:28:54	8	29	-66	-5	146	19	-30	264	81	-107	5.3	0.18	1.8	37.6	6.7
15/09/1999	15:28:54	10	7	57	36	104	5	-169	4	89	-85	8.8	0.12	2.5	11.1	5.8
15/09/1999	15:28:59	9	-3	-80	-17	145	56	-142	31	59	-41	5.4	0.13	15.5	11.1	5.5
15/09/1999	15:30:03	9	-9	53	38	237	90	-31	327	59	-180	15.6	0.06	0.3	51.8	7.8
15/09/1999	15:51:07	10	-44	-55	-1	72	61	-121	303	41	-47	22.1	0.09	1.0	31.7	5.4
15/09/1999	16:16:53	9	17	50	33	80	77	87	272	13	101	12.4	0.09	0.3	57.0	7.1
15/09/1999	16:49:45	9	22	46	32	168	29	20	60	81	117	7.1	0.07	1.5	6.8	5.5

Step #5																
15/09/1999	20:10:00	9	-24	-76	-1	354	76	-79	137	18	-126	24.4	0.13	9.7	4.3	2.5
15/09/1999	23:02:41	8	-5	-86	-9	78	84	-95	300	8	-48	14.3	0.07	0.6	2.8	2.9
15/09/1999	23:03:35	8	-6	61	32	270	90	-72	1	18	-179	15.3	0.08	0.4	29.7	7.3
15/09/1999	23:06:17	9	-13	-71	-17	189	19	-166	86	86	-72	6.6	0.12	1.1	2.3	2.9
15/09/1999	23:08:02	10	-22	-61	-17	83	15	-12	184	87	-105	13.1	0.16	11.2	13.8	4.1
15/09/1999	23:21:23	9	-10	74	17	190	76	-110	65	24	-37	3.1	0.15	1.1	7.5	3.0
17/09/1999	9:36:41	8	9	-82	-9	328	32	150	84	74	61	12.5	0.02	0.1	457.0	11.3
Step #6																
17/09/1999	11:37:13	8	11	74	15	82	87	64	346	26	173	24.8	0.02	0.2	208.0	10.0
17/09/1999	11:37:16	7	-24	-62	-15	224	77	95	23	14	69	13.2	0.03	0.1	2200.0	17.5
17/09/1999	11:37:33	7	-16	78	5	35	18	85	221	72	92	12.9	0.02	0.1	306.0	11.0
17/09/1999	12:25:34	7	39	43	17	261	79	-110	144	23	-29	8.4	0.03	0.1	255.0	12.0
17/09/1999	15:00:38	8	41	55	4	52	50	44	290	58	130	4.9	0.13	4.8	25.0	5.8
17/09/1999	15:00:39	8	22	-75	-3	219	25	48	84	72	108	27.6	0.04	1.0	104.0	8.9
17/09/1999	15:02:40	7	1	-56	-43	35	77	44	293	48	162	9.0	0.02	0.1	17.6	5.3

Figure A1: Source mechanism plots for 56 AEs located in the floor of deposition hole DA3545G01 from the upper six excavation steps. *These mechanisms are those obtained with a dominant double-couple solution. Ordering left-to-right is as Table A1. T,P,B correspond to the orientations of the tensile, pressure and null axes respectively. x indicates the orientation of the slip vector on that failure plane. Filled circles indicate positive first motions. Open circles indicate negative first motions.*

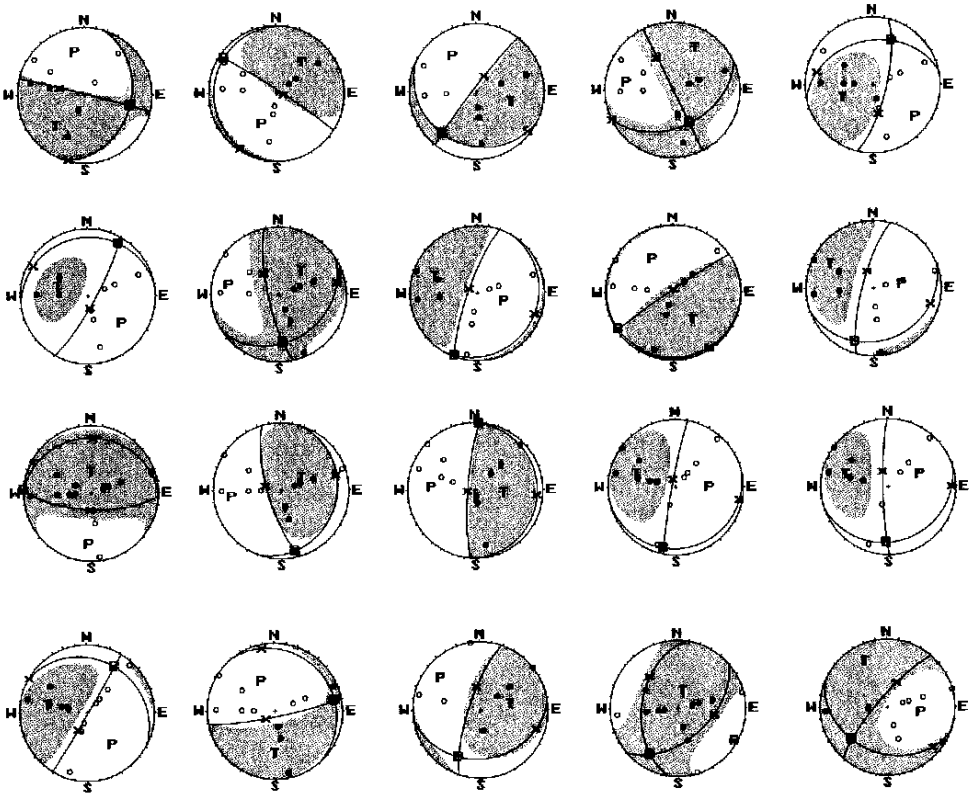

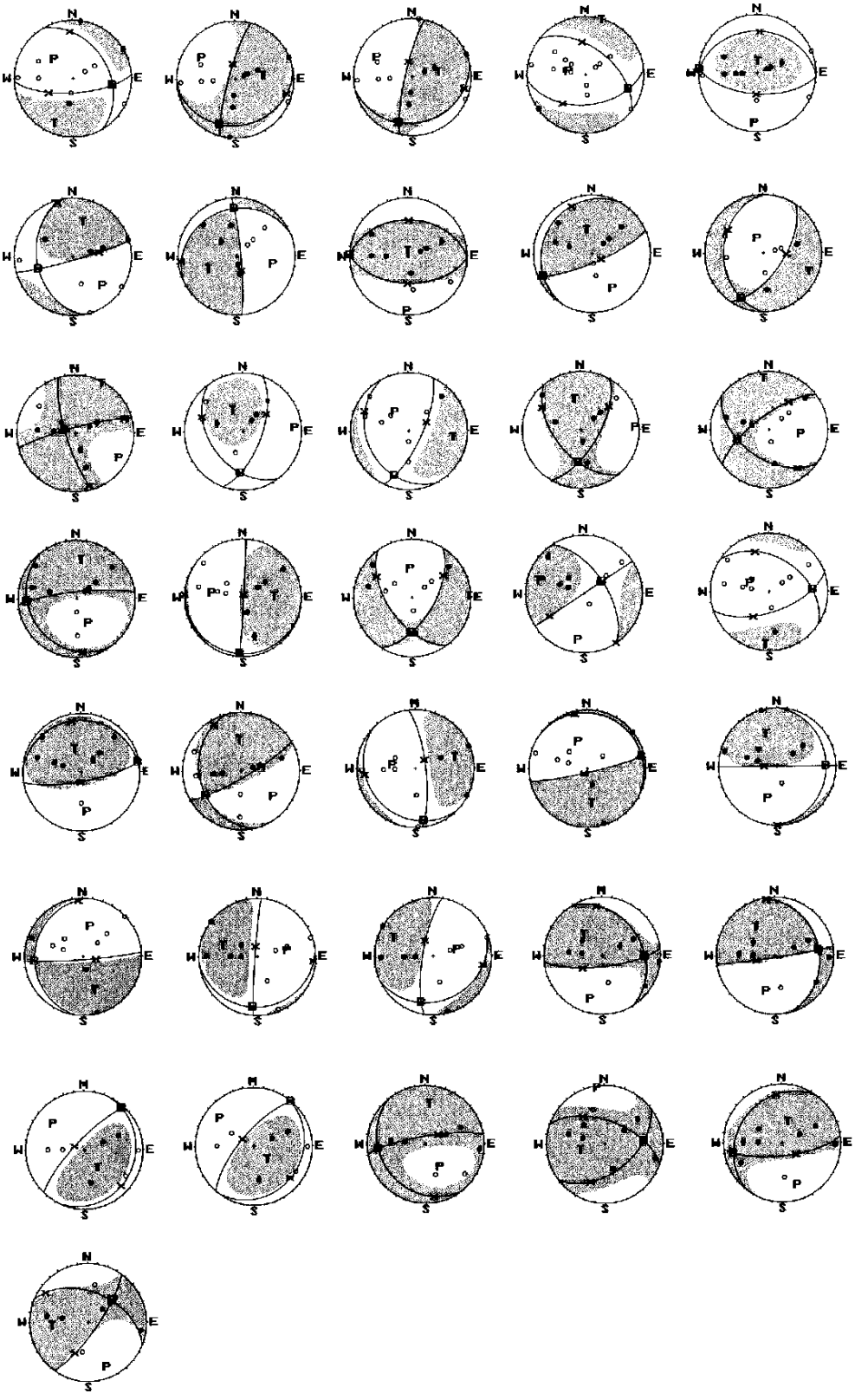
N
W
E
S
P
T

8 References

ASC, *Acoustic Emission and Ultrasonic Monitoring During the Excavation of Deposition Holes in the Canister Retrieval Test*, SKB/Äspö 03, Applied Seismology Consultants Ltd, Shrewsbury, UK, 1999a.

ASC, *Proposal for an analysis of the in situ failure criterion for Äspö Diorite*, SKB Proposal, Applied Seismology Consultants Ltd, Shrewsbury, UK, 2000b.

Baker, C., and R.P. Young, Evidence for Extensile Crack Initiation in Point Source Time-Dependent Moment Tensor Solutions, *Bull. Seismol. Soc. Am.*, *87* (6), 1442-1453, 1997.

Collins, D.S., *Excavation induced seismicity in granitic rocks: a case study at the Underground Research Laboratory, Canada*, Ph.D. thesis, Department of Earth Sciences, Keele University, Staffordshire, UK, 1997.

Collins, D.S., and R.P. Young, Lithological Controls on Seismicity in Granitic Rocks, *Bull. Seismol. Soc. Am.*, *90* (3), 709-723, 2000.

Curran, J.H., and B.T. Corkum, *Examine3D-A 3D boundary element program for calculating stresses around underground excavations in rock*, Data Visualisation Laboratory, University of Toronto, Toronto, 1993.

De Natale, G., and A. Zollo, Earthquake focal mechanisms from inversion of First P and S wave motions, in *Digital Seismology and Fine Modelling of the Lithosphere*, edited by R. Cassini, G. Nolet, and G.F. Panza, pp. 319-419, Plenum Publishing Co, 1989.

Emsley, S., O. Olsson, L. Stenberg, H.-J. Alheid, and S. Falls, *ZEDEX - A study of damage and disturbance from tunnel excavation by blasting and tunnel boring*, SKB Technical Report #97-30, SKB, Stockholm, Sweden, 1997.

Feignier, B., and R.P. Young, Failure mechanisms of microseismic events generated by a breakout development around an underground opening, in *Proceedings of the 3rd International Symposium on Rockbursts and Seismicity in Mines, Kingston, 16-18 August, 1993*, edited by R.P. Young, pp. 181-186, 1993.

Gephart, J.W., Stress and the direction of slip on fault planes, *Tectonics*, *9* (4), 845-858, 1990.

Gephart, J.W., and D.W. Forsyth, An improved method for determining the regional stress tensor using earthquake focal mechanism data: Application to San Fernando earthquake sequence, *J. Geophys. Res.*, *89* (B11), 9305-9320, 1984.

Gibowicz, S.J., and A. Kijko, *An Introduction to Mining Seismology*, Academic Press, 1994.

Hardenby, C., *Pers. Comm.*, 2000.

Jaeger, J.C., and N.G.W. Cook, *Fundamentals of rock mechanics, 3rd ed.*, Chapman and Hall, London, 1984.

Julien, P., and F.H. Cornet, Stress determination from aftershocks of the Campania-Lucania earthquake of November 23, 1980, *Annales Geophysicae*, *5B* (3), 289-300, 1987.

Leijon, B., *Summary of Rock Stress Data from Äspö*, Äspö Hard Rock Laboratory Progress Report 25-95-15, Swedish Nuclear Fuel and Waste Management Company, Sweden, 1995.

Ljunggren, C., and K.-Å. Bergsten, *Rock Stress Measurements in KA3579G*, Äspö Hard Rock Laboratory Progress Report HRL-98-09, Swedish Nuclear Fuel and Waste Management Company, Sweden, 1998.

Ljunggren, C., and H. Klasson, *Rock Stress measurements at the ZEDEX test area, Äspö HRL*, Äspö Hard Rock Laboratory Technical Note TN-96-08z, Swedish Nuclear Fuel and Waste Management Company, Sweden, 1996.

Martin, C., and N. Chandler, Stress heterogeneity and geological structures, *Int. J. Rock Mech. Min. Sci. and Geomech. Abstr.* , *30*, 993-999, 1993.

Martin, C.D., and N.A. Chandler, The Progressive Fracture of Lac du Bonnet Granite, *Int. J. Rock Mech. Min. Sci. and Geomech. Abstr.* , *31* (6), 643-659, 1994.

McKenzie, D.P., The relation between fault plane solutions for earthquakes and the directions of the principal stresses, *Bull. Seismol. Soc. Am.*, *59*, 591-601, 1969.

Nordlund, E., C. Li, and B. Carlsson, *Mechanical properties of the diorite in the Prototype Repository at Äspö HRL*, IPR-99-25, SKB, Sweden, 1999.

Ohtsu, M., Simplified moment tensor analysis and unified decomposition of acoustic emission source: Application to in situ Hydrofracturing Test, *J. Geophys. Res.*, *96*, 6211-6221, 1991.

Patel, S., L.-O. Dahlstrom, and L. Stenberg, *Characterisation of the Rock Mass in the Prototype Repository at Äspö HRL Stage 1*, Äspö Hard Rock Laboratory Progress Report HRL-97-24, Swedish Nuclear Fuel and Waste Management Company, Sweden, 1997.

Pettitt, W.S., *Acoustic emission source studies of microcracking in rock*, Ph.D. thesis, Keele University, Keele, Staffordshire, UK, 1998.

Pettitt, W.S., R.P. Young, and J.R. Marsden, Investigating the mechanics of microcrack damage induced under true-triaxial unloading,, in *SPE/ISRM Eurock '98*,Society of Petroleum Engineers Inc., pp. 509-517, 1998.

SKB, *Äspö Hard Rock Laboratory: Current Research Projects 1998*, Swedish Nuclear Fuel and Waste Management Company, Sweden, 1999.

Stump, B.W., and L.R. Johnson, The determination of source properties by the linear inversion of seismograms, *Bulletin of the Seismological Society of America* , 67, 1489-1502, 1977.

Urbancic, T.I., C.-I. Trifu, and R.P. Young, Microseismicity derived fault-planes and their relationship to focal mechanism, stress inversion, and geologic data, *Geophys. Res. Lett.*, *20* (22), 2475-2478, 1993.

Young, R.P., J.F. Hazzard, and W.S. Pettitt, Seismic and micromechanical studies of rock fracture, *Geophys. Res. Lett.*, 27 (12), 1767-1770, 2000.

Young, R.P., C.D. Martin, R. Murdie, J. Alcott, S. Falls, I. Stimpson, and S. Yazici, *Numerical Modelling, Acoustic Emission and Velocity Studies of the Excavation Disturbed Zone at the Hard Rock Laboratory*, Äspö Hard Rock Laboratory Technical Note, Swedish Nuclear Fuel and Waste Management Company, Sweden, 1996.